

Universidad de Sevilla

Facultad de Biología

Dept. de Biología celular



Scutoids unveil the three-dimensional packing in curved epithelia

Tesis doctoral en el programa de Biología integrada por la
Universidad de Sevilla

Pedro Javier Gómez Gálvez

Sevilla, 2020

Doctorando

A handwritten signature in blue ink, consisting of a series of loops and a long horizontal stroke at the end.

Pedro Javier Gómez Gálvez


Director/Tutor

A handwritten signature in blue ink, featuring a large, stylized 'L' and 'M' followed by a horizontal stroke.

Luis María Escudero Cuadrado

AGRADEDECIMIENTOS

Un conjunto de casualidades me llevó a tomar el camino de la investigación, siendo una oportunidad para iniciarme en el ámbito laboral. Iluso de mí, que no conocía como funcionaba este sector. Sin embargo, pronto descubriría que el fin que se persigue es más noble y altruista que en cualquier trabajo empresarial.

Una de estas casualidades tiene nombre y apellidos: Luis María Escudero Cuadrado. Él apostó por mí para comenzar a construir un equipo de investigación, comprometiéndose a dirigir y financiar mi tesis doctoral aun cuando la viabilidad económica del grupo era muy incierta. De esto hace ya 4 años. Puedo decir que ha cumplido todo, y con creces. Valoro lo que hace por nosotros, como lo hace, y los ideales que defiende desde la sencillez. Siempre preocupándose por todo el grupo, trabajando para que no nos quedemos sin financiación y luchando para que el laboratorio siga funcionando (aun estando de baja paternal). Su cercanía hace que le trate como a un amigo con el que bromear o con el que puedes hablar sobre cualquier asunto personal, saliéndose del estereotipo de jefe estricto que solo piensa en el trabajo. Esto produce un exceso de confianza que, a veces, hace que nos pasemos un poco de la raya. Seguro que no se le olvidará cuando nos pilló el grupo secreto de Whatsapp cuyo nombre representa su Kryptonita: “Antibióticos y proLego” . Una suerte y un orgullo tenerle como director de tesis, mentor y amigo.

Aunque Luisma ha sido el que me ha guiado en todo este camino, muchas son las personas que me han acompañado, han compartido vivencias y me han ayudado desde el principio. Está claro que con unas meras palabras es imposible agradecer suficientemente lo que han hecho por mí, pero, al menos, haré mención de todos y cada uno de ellos: desde mi predecesor Dani (coincidí con él solo un día, y actualmente sigo odiando su código) hasta todos los estudiantes de prácticas (Pedro, Chiara, Óscar y Víctor), TFG (Veredas, Marina, Elena, Cristina, Carolina y Pepe) o TFM (Marta y Álvaro) que han pasado por el laboratorio.

Por supuesto, debo dar las gracias a todos los miembros actuales y antiguos del lab:

- A Antoñito, que siempre será ‘the last monkey’ del lab por muchos méritos que acumule y aunque aprenda a programar.
- A Charlie y a sus antichistes, en especial al del payaso Pagliacci. Perdóname por transformar tu “Iniestazo” en el “Robo de Stamford Bridge”.
- A Ana Castro y Tina un par de frikis de las buenas que dejaron una gran marca en el laboratorio.
- A Carmen y Ana Palacios las chicas del laboratorio del IBiS, que, aunque no coincidamos en el día a día, cada vez que nos juntamos somos una piña.
- A la jefa Valentina y Bea, que le han dado un soplo de aire fresco al departamento y han traído alegría y conocimiento al grupo.

Merece un especial agradecimiento mi compañero Pablo. Él me ha tenido que aguantar todos los días desde que llegó al lab. Ha sido mi compañero de batallas, de alegrías y sufrimientos. Puede ser la persona más peculiar que haya conocido. Su forma de ser y de pensar es muy diferente a la mía, quizás eso es lo que ha hecho que ahora seamos tan amigos. Podría contar mil anécdotas de todo este tiempo juntos, pero solo dejaré una frase que él entenderá, “¿te imaginas a...?” ;). Gracias por todo.

También agradecer su cariño al resto de personas que me han acompañado durante estos años en el departamento de Biología: a Reme, nuestra madre del departamento que con sus visitas llenaba de alegría el laboratorio; a Ana Mari que fue mi única compañía predoctoral durante los primeros meses; a Auxi, Sergio, Susana y Sofía que hacen que la hora de la comida sea el momento más ansiado del día. Sin olvidar al resto de profesores y a la dirección del departamento que nos han acogido desde nuestra llegada como si fuéramos de la familia.

Gracias al laboratorio 109 del IBIS con los que tenemos un vínculo especial dentro y fuera de la ciencia, y gracias a todos los colaboradores del grupo, en especial a Alberto Márquez, Clara Grima y Javier Buceta.

Por último y más importante, agradecer todo lo que mi familia ha hecho por mí. A mis padres que en la distancia me han apoyado en cada momento y son los principales responsables de que yo me haya convertido en la persona que soy. Gracias mamá por los tupperts de lentejas, que siempre están espectaculares. A mis hermanos que en mayor o menor grado han estado vinculados con el mundo de la ciencia y entienden lo complicado que es este camino. Seguramente parte de culpa de que yo me encuentre realizando una carrera investigadora la tenga mi hermano mayor. Él anduvo este camino antes que yo y quizás inconscientemente haya seguido sus pasos. Por cierto, un diseño de fantasía el que ha hecho para la portada. Por último, a mi pareja, Inma, una de las personas que más valoro en todos los sentidos. Ella es la que está viviendo de cerca toda esta etapa de mi vida y es un pilar fundamental que me aconseja y me guía para que siga adelante. Gracias por ser así.

MUCHÍSIMAS GRACIAS A TODOS.

SUMMARY

As animals develop, the initial simple planar epithelia of the early embryos must acquire complex three-dimensional architectures to form the final functional tissues of the organism. Epithelial bending is, therefore, a general principle of all developing systems. Scholarly publications depict epithelial cells as prisms where their basal and apical faces resemble polygons with the same number of sides. The accepted view is that, when a tissue bend, the cells of the epithelia modify their shape from columnar to what has been traditionally called “bottle shape”. However, the morphology and packing of curved epithelia remain largely unknown. Here, through mathematical and computational modelling, we show that cells in bent epithelia necessarily undergo intercalations along the apico-basal axis. This event forces cells to exchange their neighbours between their basal and apical surfaces. Therefore, the traditional view of epithelial cells as simple prisms is incompatible with this phenomenon. Consequently, epithelial cells are compelled to adopt a novel geometrical shape that we have named “scutoid”. The in-depth analysis of diverse epithelial tissues and organs confirm the generation of apico-basal transitions among cell during morphogenesis. Using biophysics arguments, we determine that scutoids support the energetic minimization on the tissue and conclude that the transitions along the apico-basal axis stabilize the three-dimensional packing of the tissue. Altogether, we argue that scutoids are nature’s solution to bend efficiently epithelia, and the missing piece for developing a unifying and realistic model of epithelial architecture.

INDEXES

GENERAL INDEX

FIGURES INDEX	I
ABBREVIATIONS AND GLOSSARY	II
INTRODUCTION.....	
1.1. The development of patterns in living organisms.....	2
1.2. Epithelial tissues.....	3
1.3. <i>Drosophila melanogaster</i> as a biological model.....	5
1.4. Packed tissues and mathematical tessellations.....	9
1.5. Organization principles during epithelial morphogenesis	10
1.6. The complexity of the three-dimensional packing in epithelia	15
OBJECTIVES.....	18
MATERIALS AND METHODS.....	22
3.1. Conceptualization of Voronoi diagrams on parallel curved surfaces.....	24
3.2. Computational models.....	25
3.3. Biological models	29
3.4. Biophysical model – line tension minimization model.....	31
3.5. Statistics and illustrations.....	31
RESULTS	34
4.1. A Voronoi tubular model unveils cells exchanging its neighbours along the apico-basal axis.....	36
4.2. Analysing the scutoids presence in epithelial tubes.....	38
4.3. A general fact: the curved epithelia hold scutoidal cells	45
4.4. Voronoi spheroidal models reproducing egg chamber structures.....	49
4.5. A biophysical model to analyse the apico-basal intercalations	52
DISCUSSION	56
CONCLUSIONS	66
ANNEXE.....	70
BIBLIOGRAPHY.....	74

FIGURES INDEX

Figure 1. Natural patterns.....	2
Figure 2. Epithelial cells scheme	5
Figure 3. Life cycle – <i>Drosophila melanogaster</i>	6
Figure 4. Confocal section of the salivary gland of wild type <i>Drosophila melanogaster</i>	7
Figure 5. <i>Drosophila</i> egg chamber development	8
Figure 6. Voronoi diagram and packed tissues.....	9
Figure 7. Epithelial biophysics	12
Figure 8. Centroidal Voronoi Tessellation (<i>CVT</i>) path	14
Figure 9. Epithelial 3D shapes and <i>T1</i> transition	17
Figure 10. Voronoi tubular model.....	37
Figure 11. Tracking salivary gland confocal stacks	39
Figure 12. Voronoi tubular model screening	40
Figure 13. Quantification of neighbours exchanges	41
Figure 14. Geometric measurements from intercellular edges	42
Figure 15. Measurements of transitional edge lengths and angles from apical.	44
Figure 16. Scutoids found in <i>Drosophila</i> embryo	46
Figure 17. Scutoids presence in <i>Drosophila</i> egg chamber	47
Figure 18. Scutoids are found in zebrafish epiboly.	48
Figure 19. Voronoi spheroidal models.....	50
Figure 20. Voronoi spheroidal models imitating the egg chambers at stage 4 and 8 of development.....	51
Figure 21. Line-tension minimization model applied to epithelia	53
Figure 22. Tracking of energetic states	54
Figure 23. Energetic trajectories in egg chambers and its associated models	55
Figure 24. Summary of three-dimensional packing assuming at least a null curvature.....	62
Figure 25. General 3D model considering 3 positive degrees of curvature	63

ABBREVIATIONS AND GLOSSARY

Ch: Cells height.

CVT path: “Centroidal Voronoi Tessellation path”. A quantitative scale of epithelial organization developed in (Sanchez-Gutierrez et al., 2016).

DAPI: (4',6-diamidino-2-phenylindole). Fluorescent stain for DNA.

E: Energetic state of a four-cells motif in terms of line-tension energy. This energetic state could be divided into two sub-energetic states: E_w or E_h , for the four-cells motifs configurations S_w and S_h respectively.

h: Height of a four-cells motif (**Figure 21A**).

K: Curvature.

k₁: Curvature in Prime Vertical in an ellipsoidal surface.

k₂: Curvature in Meridian in an ellipsoidal surface.

l: Intercellular edge length of a four-cells motif.

L_T: Sum of all the edges length into a four-cell motif packing configuration (**Figure 21A**).

R_b: Basal radius. Cylindrical radius to the basal surface.

ROI: Region of interest.

SR: Surface ratio. It determines the difference of curvature in a tube with the non-dimensional formula: R_b/R_a . If R_a is larger than R_b , then the surface ratio should be defined as R_a/R_b .

Std: Standard deviation of the mean value.

S: Four-cells motif state that could be subdivided in S_w if $w > h$, and S_h if $h > w$.

S4: Stage 4.

S8: Stage 8.

T1: Transition 1. Morphogenetic movement, where the cells exchange its neighbours along the time.

w: width of a four-cells motif (**Figure 21A**).

WT: Wild type. The standard and common phenotype of a species without induced mutations.

3D: Three-dimensional.

ε: Aspect ratio of a four-cells motif $\left(\frac{h}{w}\right)$.

INTRODUCTION

1.1. The development of patterns in living organisms

In nature, we can find lots of natural structures organized in patterns: fractals, stripes, symmetric elements, cracks, tessellations... (**Figure 1**). The circulatory system of animals, the clouds, the snowflakes or the structure of some plants are examples of natural fractals (**Figure 1A**). The skin of tigers or zebras is covered by stripes that give an organized pattern of two colours (**Figure 1B**). Tessellations are formed by a set of tiles (basic structural unit) that assemble without leaving empty gaps between them and without overlapping. They can be found in some parts of nature from honeycombs (**Figure 1C**) to tortoise shells or epithelial tissue. Besides the mentioned patterns, in nature, it can be observed symmetric elements at different scales. Symmetry is a result of evolution, and it is an important factor for classifying animal taxonomy. Starfishes own a radial symmetry meanwhile the human body is bilateral: the left side could be a mirrored of the right side (**Figure 1D**).

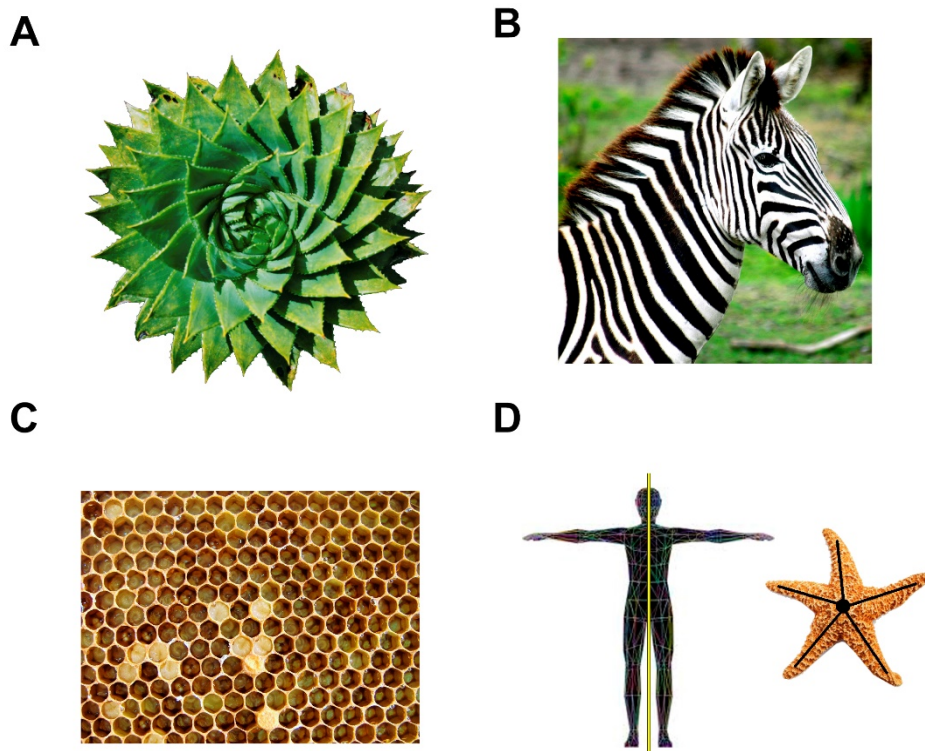


Figure 1. Natural patterns

A) Fractal plant with spiral conformation. **B)** Zebra with striped skin. **C)** Honeycomb hexagonal lattice. **D)** Bilateral and radial symmetry, of humans and starfishes respectively. Edited images obtained from <https://pxhere.com> without attribution required.

In living organisms, these geometrical features emerge due to the self-arrangement of cells and tissues during their development. Understanding how these complex living structures build-up from the embryonic stages is a key question to understand the fundamentals of life. How do the organisms grow and develop? Developmental biology is the scientific discipline responsible for studying the morphogenetic processes, how the cells grow, divide, migrate, differentiate and the factors responsible of regulating these events; how a zygote can reach functional complex structures forming an organism with vital functionality by following genes instructions.

Definitively, nature is closely linked with organization and its study in relation to developmental biology could unmask the intrinsic mechanisms that lead to living matter stability.

1.2. Epithelial tissues

The animals are constituted by four fundamental types of tissues: connective, muscle, nerve and epithelial. The epithelium is an avascular tissue composed by one or several layers of cells adhered between them. These cells, considered as the building blocks of metazoans, cover external surfaces of the organs, inner and outer cavities, viscera, in addition to forming ducts and are a main component of secretory glands.

The cells forming the epithelial tissue are characterized, in general, by being closely joined to one another without leaving empty space between them. In this way, the cells are linked through special intercellular connections, called “tight junctions”, besides the basement membrane that performs as connective tissue. Another main feature of epithelial cells is the polarity, distinguishing three different regions in the cell structure. Considering a monolayer of epithelial cells, we find: the apical region, oriented to the external surface, or the lumen or cavity of an epithelial duct; the lateral region, contacting with the neighbouring cells through different adhesion molecules, and the basal region, being the opposite part to the apical section, where the cell is fixed to the underlying conjunctive tissue.

The epithelial cells can be classified into three main groups based on their shapes (**Figure 2**):

- Squamous cells. Consists of acutely thin cells so much longer in width than height.
- Cuboidal cells. This type of cells looks like cubes with a similar size along the cellular width and height.
- Columnar cells. Stands for elongated cells along its longitudinal axis.

Simultaneously, epithelia can also be categorized depending on mono- or multi-layering organization (**Figure 2**):

- Simple epithelia are single layers of epithelial cells that maintain direct contact with the basal membrane and share the apical surface. Either the squamous, the cuboidal or the columnar cells can be the main components of these monolayers.
- A stratified epithelium is defined as one or more of epithelial cells layers stacked over a unique one that is contacting with the basement membrane; in like manner, the apical surface of only one layer is exposed to the inner organ cavity or the outside environment.

A special subset of stratified epithelia are the transient epithelia that change their cellular shapes depending on the internal pressure of the organs, and they are exclusive of the excretory system.

- A variant of these tissue archetypes is the pseudostratified epithelium. This type of epithelial tissue is a simple epithelium with the peculiarity of their nuclei being placed at different levels of height, producing a false perception of being a multilayer epithelium.

Independently of its architecture, these multi or monolayers might be present in the organism as lining tissue or developing endocrine/exocrine functions in glands (**Figure 2**). The functions of the diverse types of epithelia span from enclosing and protect the vital body components, produce excretions or secretions, or working in selective absorption. During the embryonic development, the cells present epithelial characteristics. In the adult animal, epithelia cover most of the organs and the body surfaces (gastrointestinal tract, skin, eyes, liver, lungs, spinal cord, etc.), and are the principal component of the secretory glands of the organism.

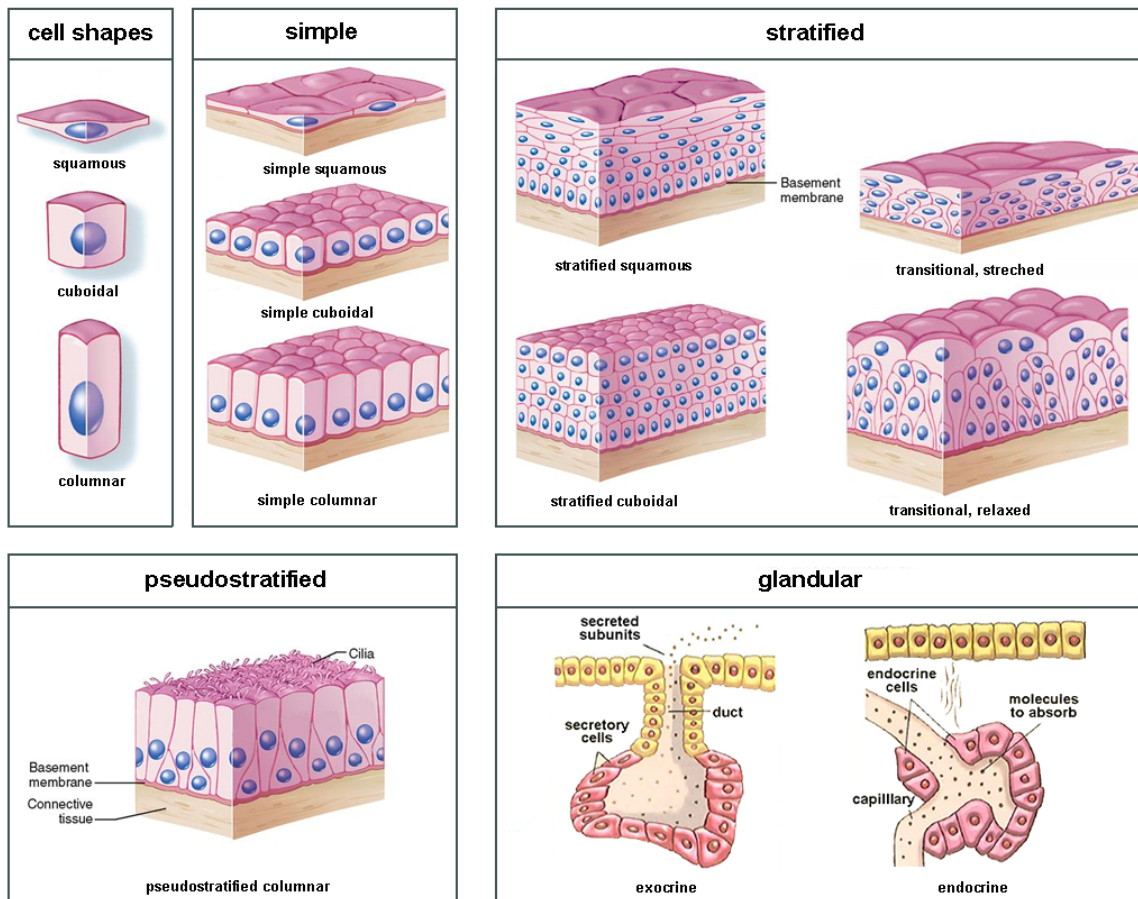


Figure 2. Epithelial cells scheme

The illustration shows up the different types of epithelial cells: squamous, cuboidal or columnar. Besides, representing how these building blocks can be grouped as simple, stratified, pseudostratified or glandular epithelia. Edited images from (Tortora and Derrickson, 2018; Villanueva et al., 2003).

This section has been constructed as a compendium of different sources (Kahle et al., 2013; Kondo and Hayashi, 2015; O'Toole, 2009; Ross and Pawlina, 2012; Welsch et al., 2014).

1.3. *Drosophila melanogaster* as a biological model

The *Drosophila melanogaster* is a model organism highly used in developmental biology for more than one century. The commonly known as fruit fly is a holometabolous insect, that is to say, carries on the full metamorphosis. At room temperature (25 °C) an embryo gets to its adult stage after 10 days (**Figure 3A**) and could be conserved into test tubes (**Figure 3B**) (Gramates et al., 2017).

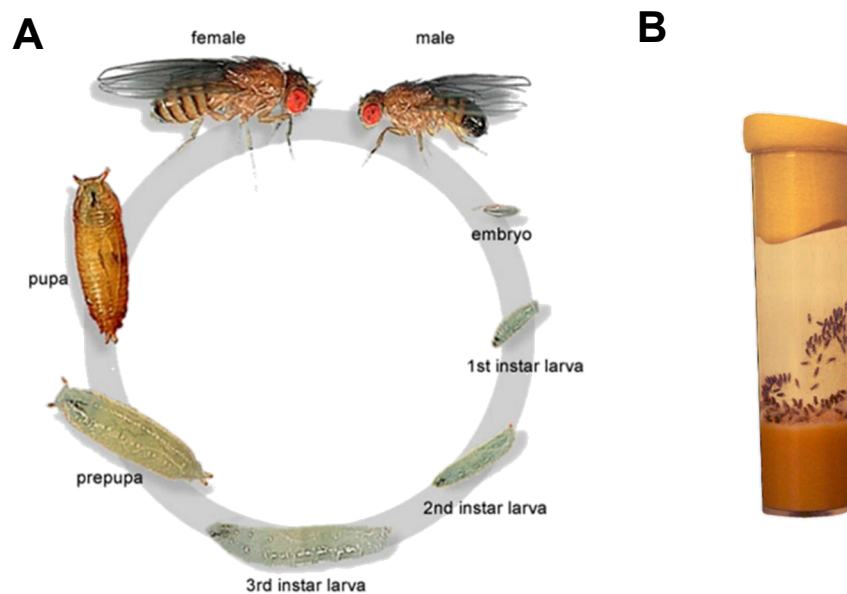


Figure 3. Life cycle – *Drosophila melanogaster*

A) At 25°C: 1-day embryogenesis; 1-day 1st instar larva; 1-day 2nd instar larva; 2-3 days 3rd instar larva and 5 days at the pupal stage before adult fly. Female adults have dark bands on the abdomen, and the males only have the abdomen extreme in a dark tone. Edited image from (Weigmann et al., 2003). **B)** Tubes where the *Drosophila melanogaster* are conserved in a laboratory. Edited image from https://es.wikipedia.org/wiki/Archivo:Drosophila_melanogaster_laboratory_culture-vial.jpg.

Drosophila has been used as a model in a large number of molecular and cellular processes since a wide range of mechanisms and biological pathways have been conserved along the evolution (Bier, 2005; Dahmann, 2008; Gramates et al., 2017; Jennings, 2011). Comparing the genomic maps of humans and *Drosophila*, it has been calculated that around the 61% of genes involved in human diseases present a counterpart in the fly genome (Adams et al., 2000). This insect has a short life cycle with a high offspring that empowers the realization of genetic crosses quickly and efficiently (Bier, 2005). The usage of this type of model present another bunch of advantages such as: a small size that provide its manipulation and storage in confined space; its low cost; the absence of ethical concerns; a reduced number of genes in relation with the vertebrates and a high quantity of genetic tools produced by the scientific community. The latter makes very easy to alter the function of particular proteins and the study of dynamic events (Bulgakova et al., 2012; Jiménez and Merchant, 2003; Rodriguez-Arnaiz et al., 1992).

1.3.1. Salivary glands

One of the principal tissues analysed throughout this project has been the salivary gland of *Drosophila melanogaster* third instar larvae. The main advantage provided by this type of epithelial tissue is related to the easy dissection and isolation from the rest of the organs. Also, with the support of a confocal microscope, it is not complex to obtain high-quality images to quantify their epithelial architecture.

These tissues own a special characteristic: since they differentiate themselves without the appearance of cellular divisions and apoptosis, it grows just increasing the volume of pre-existing cells. Hence, it has been eliminated some concerns regarding factors regulating mitosis and controlling cell division or about programmed cell death, doing simpler the analysis of organ development (Andrew et al., 2000). Generally, the salivary glands adopt a cylindrical shape, where the basal region of the secretory cells demarcates the external surface of the organ, while the apical regions are placed surrounding the gland lumen (also with cylindrical shape) (**Figure 4**).

The salivary glands are connected to the anterior part of the intestine being essential organs for the digestion. They are composed of secretory and ductal cells, both of cuboidal shape. The ductal ones build the tube that connects the larvae mouth with the secretory cells, that synthesize and release the proteins inside the gland lumen to digest the food (Andrew et al., 2000; Weigmann et al., 2003). Besides, these organs have

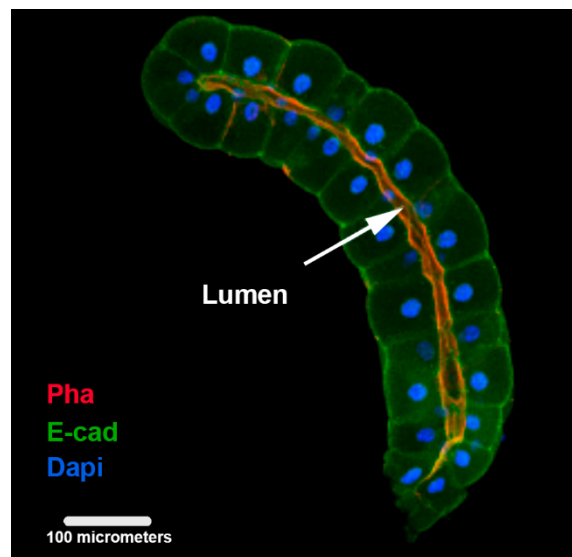


Figure 4. Confocal section of the salivary gland of wild type *Drosophila melanogaster*

The chromatin of the cell nuclei has been stained with DAPI (blue), the E-cadherin adhesion molecule in green, the red staining is the Phalloidin marker with affinity to the F-actin. The white arrow points to the gland lumen. The white bar at the bottom left represents a length of 100 micrometres.

another fundamental function at the beginning of the metamorphosis, secreting an adhesive to fix the fly puparium (an outer jacket that covers the pupa) to the substrate.

1.3.2. Egg chambers

The egg chamber is a basic developmental element of oogenesis that will give rise to the mature egg of *Drosophila*, and it is located on the ovaries of adult female flies (Gates, 2012). There are 6 or 7 egg chambers per ovariole, 16 ovarioles per ovary and 2 ovaries per female fly. The set of 6/7 egg chambers are fettered between them through somatic cells, and they begin the mature develop sequentially (**Figure 5**). This developmental process is constituted by 14 stages until completing the ripening. At the first stages the structure holds a spherical shape that elongates over the growth stages to an ellipsoid with a final major/minor axes ratio of 3 (Jia et al., 2016).

Particularly, each egg chamber contains 16 germ-line cells, the oocyte and fifteen nurse cells that support the oocyte development. These cells are surrounded by a simple layer of somatic cells, the follicular cells (Spradling, 1993) getting an oval three-dimensional shape. The apical part of these cells is internally contacting with the oocyte and the nurse cells, while the basal surface limits with the exterior. During the oogenesis, these cells go through different developmental cycles: between the stages 1 and 6, the cells are involved in the mitotic cycle, from 7 to 10A they enter in endocycle and later only occur gene amplification (Jia et al., 2016).

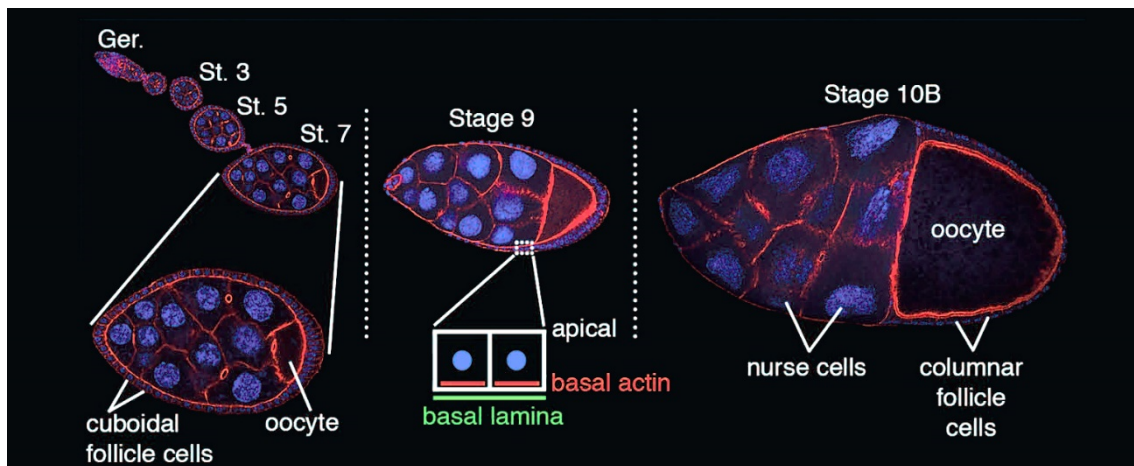


Figure 5. *Drosophila* egg chamber development

A sequence of egg chamber at different stages. F-actin is stained with phalloidin in red colour and the DNA with DAPI in blue. The images represent the central single plane of egg chambers, showing the follicle cells, the nurse cells and the oocyte. At left it is displayed a sequence of linked egg chambers in development from the germarium to the stage 7. More advanced stages (9 and 10B) are shown isolated at the centre and at right. Adapted from (Gates, 2012).

The follicular cells have been commonly used as a biological model to research the regulation of the cell cycle, differentiation (Artavanis-Tsakonas et al., 1999), polarity (Lewellyn et al., 2013), endo- and exocytosis (Coutelis and Ephrussi, 2007; Vaccari et al., 2008) or cancer (Jang et al., 2007).

1.4. Packed tissues and mathematical tessellations

The epithelia can be considered as natural tessellations when they are simplified and reduced to one of their surfaces. That means, that their cells are closely arranged without overlap and not allowing empty space between them. In these images (**Figure 6**), epithelial cells appear perfectly packed, in a similar way to mosaics or tessellated patterns.

A Voronoi diagram or Voronoi tessellation is a mathematical concept based on compartmentalizing or clustering the Euclidean space by proximity, in which each compartment is called Voronoi cell. Interestingly, Voronoi tessellations present a similar aspect to most epithelial surfaces (**Figure 6**). For developing a Voronoi diagram are necessary two indispensable elements, a set of seeds that are the source for each Voronoi cell and a defined space where the tessellation process will take place. From each seed will emerge a Voronoi cell filling the surface preventing gaps among the cells, and not allowing overlapping between the regions, resulting in a subdivision of convex polygons. The rule that prevails in this mathematical assumption is defined by: a Voronoi cell will contain all the coordinates closer to its seed than any other seed (Voronoi, 1908) (**Figure 6**).

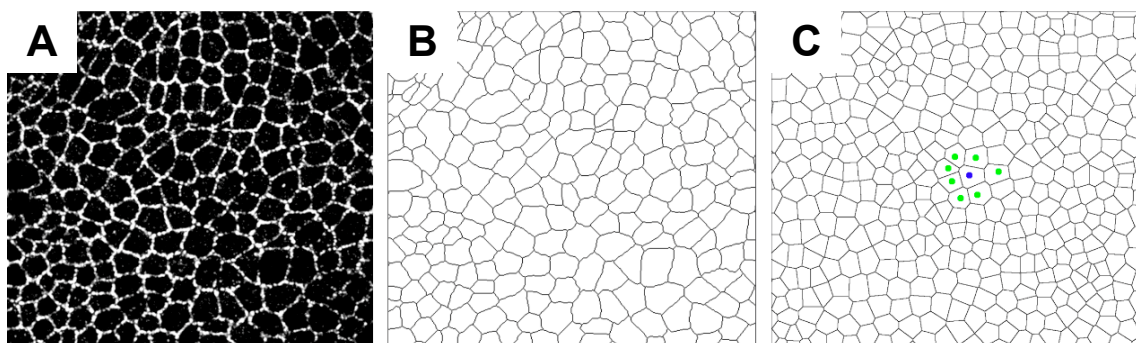


Figure 6. Voronoi diagram and packed tissues

A) Epithelium of third instar *Drosophila* imaginal disc (Vicente-Munuera et al., 2019a). **B)** Segmented image of A. **C)** Voronoi diagram emerged from a set of seeds, where a Voronoi region is delimited by the closest coordinates to its seed (the coordinates into the region emerged from the blue seed are closer to the cited seed than the surrounding green seeds).

Both the packed tissues and the Voronoi diagrams are tessellations composed by an entire collection of convex polygonal cells, and intrinsically follow a set of arrangement laws or theorems:

- From the Euler formula where it is correlated the number of vertices (V), edges (E) and faces (F) of polygons with the Euler number (2): $V - E + F = 2$ (Euler, 1767), K. Reinhardt extrapolated a formal explanation on polygonal tessellations where explain how the average number of polygonal sides of a fulfilled tessellation should be approximately 6 (Reinhardt, 1918). This assumption was experimentally tested by Wetzel in epithelia (Wetzel, 1926). In biological terms, the average number of neighbouring cells in a natural tessellation (i.e. epithelium) will tend to 6.

$$\bar{n} = \sum_{i=1}^N \frac{n_i}{N}, \quad \bar{n} \sim 6$$

\bar{n} is the average number of sides per cell, where n_i is the number of sides in a cell i . N is the total number of cells.

- Lewis developed a law quantifying cells area in the epidermal layer of cucumbers and established a relationship between cellular areas and its number of neighbours (Lewis, 1928). Lewis found that the mean area of cells with the same number of neighbouring cells described approximately a linear function. Namely, the larger the area the greater the number of neighbours. Thus, smaller cells would tend to have a minor number of neighbours.

$$A_n = \frac{A_0}{N} \cdot (n - 2)$$

A_n is the average apical cell area, in which, n is the number of its edges. N is the total number of cells, and A_0 the total apical surface area.

These laws, among others, enable to examine the mathematical principles in relation to biological traits. They have been essential to advance in the knowledge of the natural tessellations properties, for example, supporting the study of the epithelial grow dynamics or how packed tissues organize (Escudero et al., 2011; Heller et al., 2016; Kokic et al., 2019; Sanchez-Gutierrez et al., 2016).

1.5. Organization principles during epithelial morphogenesis

The previous subsection showed that the epithelial organization follow several mathematical laws. How cells arrange along the epithelia is a concept widely studied, and this has been an object of study for long years in mathematics and biology fields (Haeckel, 1904; Stevens, 1974). This branch of research tries to comprehend and

explain essential morphogenetic processes along the development of an organism, such as gastrulation, control of tissue shape and size, convergent extension or the formation of the organ. From this context, lots of researches have made use of geometrical concepts to understand how the tissues architecting and reorganizing to be functional (Chichilnisky, 1986; Classen et al., 2005; Hayashi and Carthew, 2004; Honda, 1978). One of the most common geometrical/topological tools that have been used in biology to unmask the basis of the morphogenetic procedures is the polygon distribution analysis, in which the tissue cells are assumed convex polygons (Farhadifar et al., 2007; Gibson et al., 2006; Sanchez-Gutierrez et al., 2016; Shraiman, 2005).

1.5.1. Polygon distribution as a hint to quantify the epithelial organization

The topology of the apical layers in epithelia have been well studied along with metazoa development. From the beginning of the 20th century when Frederic T. Lewis used the polygon distribution to study the epidermal in *Cucumis* (Lewis, 1928), more and more researchers have coined it as a valuable tool to investigate the manner in which epithelia are organized (Gibson and Gibson, 2009; Gibson et al., 2006; Korn and Spalding, 1973). Some works defend that the preserved polygon distribution in the same type of epithelial tissue is a consequence of the proliferation explained with a stochastic model, the Markov Chain (Axelrod, 2006; Gibson et al., 2006), jointly with the tissue rearrangements due to transitional cellular movements (Aegerter-Wilmsen et al., 2010; Classen et al., 2005; Zallen and Zallen, 2004). Other complementary methods combine the polygon distribution analysis with the application of *in silico* models: Voronoi diagrams or Vertex models approaches, among some other, trying to reproduce and explain the biological behaviour by simply means of mathematical/computational simulations (Aland et al., 2015; Bi et al., 2016; Curran et al., 2017; Farhadifar et al., 2007; Vicente-Munuera et al., 2019b). For example, a recent work of our group using this technique defends that the conserved polygon distribution is not exclusively dependent on the cell division mechanisms, giving more importance to the turgidity between the cells (Sanchez-Gutierrez et al., 2016).

1.5.2. Vertex model mimicking the physical properties of the epithelium

The understanding of the different processes along with the tissue formation, attach importance to the description of the homeostatic conditions that make possible the correct functionality of the final tissue. In this way, it is essential to study the dynamics and the interactions between the cells. This could help in the identification of pathologic behaviours as possible precursors for an illness. In the developmental biology field, the *vertex model* is a popular simulation method that reflects by computation the intrinsic

biophysics of a dynamic model, imitating the biological events (Bi et al., 2016; Farhadifar et al., 2007; Fletcher et al., 2014; Hardin and Walston, 2004; Sanchez-Gutierrez et al., 2016).

These computational simulations, having the capability of resembling forces balance within the epithelium, provide support to the genetic studies and the imaging that attempts to define the mechanisms operating in cell sheet dynamic. The *vertex model* framework is based on polygonal objects that represent the cellular interfaces, in which the vertices are placed linking the edges shared by the adjacent cells. This modelling simulates a steady-state force balance, in which three forces' components act over the vertices (**Figure 7**).

The three contributors to the potential energy $E(R_i)$, in a particular configuration of the epithelial junctional network, are area elasticity, line tension along apical junctions, and contractility. This biophysical function evaluates the deformation conditions of the cellular areas to change its shape, along with the tension and adhesion between the cells: the

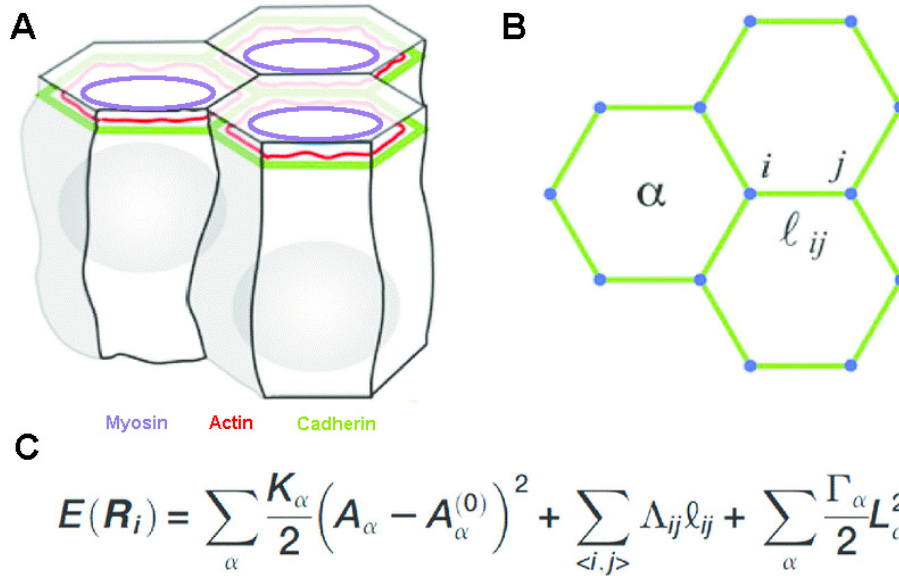


Figure 7. Epithelial biophysics

A) Sketch of three cells, representing the adherence junctions (green) and the actin-myosin bundles (red and blue). **B)** Simplified 2D vision of the apical surface, considering the cells as joined hexagons constructed with edges (green, ℓ_{ij}) and vertices (blue, numbered by unique ids i, j), being α the cell id. **C)** Minimization of the energetic equation in mechanical equilibrium considering R_i as the 2D location of the i vertex. K_{α} is the elasticity, and A_{α} the area of the cell α . Λ_{ij} the line tension of the edge connecting the i and j vertices, where ℓ_{ij} is the length. Γ_{α} is the contractility of the cell α , and L_{α} denoted the cell perimeter. Edited illustration from (Farhadifar et al., 2007; Kong et al., 2017).

first and second equation terms. Meanwhile, the third term is more related to the inner cell pressure or its tendency to growth (**Figure 7C**).

Likewise, the previously mentioned force components could be associated also with the biological performance of several cell molecules. Indeed, it has been described that E-cadherin (Lecuit and Lenne, 2007), a type of cell adhesion protein related to the adherence junction formation, is directly responsible for cell adhesion force. Also, it has been established that the myosin-II actin filaments, that embody the cell cytoskeleton, control the cortical tension and regulate the cell contacts. The cellular movements depend on the cell polarity that is associated to some proteins, the E-cadherin, the actomyosin filaments or the β -catenin (support the anchorage of the cadherin with the actin cytoskeleton) among others (Lecuit and Lenne, 2007). All that, relates the physics and the biology of the cells, just what the vertex model try to explain.

Hence, the vertex model together with suitable biological samples (for example, the wing disc of *Drosophila*), have been very useful models that allow studying different processes along with the epithelial development from a biophysical point of view. The polarity and cellular migration, the cell division, the adhesion between the cells, the delamination or simply the epithelium growth have been some of the targets of study since the vertex model appearance (Canela-Xandri et al., 2011; Farhadifar et al., 2007; Fletcher et al., 2014; Mao et al., 2013; Sanchez-Gutierrez et al., 2016). At this point, we have shown the basis of the vertex models with its traditional three main force parameters. Notwithstanding, this biophysical-computational tool is continuously evolving, integrating new force considerations, cells interactions, being adjusted to three-dimensional environments and combined with other validated methodologies to study complex morphogenetic events, for example, branching growth (Okuda et al., 2018) or tissue super-elasticity (Latorre et al., 2018).

1.5.3. Voronoi diagrams as a model to study the epithelial organization

Since the second half of the last century, some studies tried to analyse different cellular patterns observed in nature by employing the Voronoi diagram as a mathematical model (Gibson and Gibson, 2009; Hočevár et al., 2010; Honda, 1978; Zhu et al., 2001).

In 1978, Honda and cols. studied several natural tessellations (the epithelial tissues among others) using these diagrams. They used the centre of mass of each epithelial cell to emerge a Voronoi cell and demonstrated that these mathematical patterns well-fitted how the epithelia were organized along planar surfaces (Honda, 1978). Afterwards, more recent articles also defend that the apical surface of the epithelial layers is

topologically disposed following the organizational principles of Voronoi diagrams, formed by very regular polygons with a high proportion of 6-sided cells (Gibson and Gibson, 2009; Hočevár et al., 2010; Sanchez-Gutierrez et al., 2016; Zhu et al., 2001). On this wise, theoretically, the Voronoi diagrams can be considered as a tool with capabilities to unmask the subjacent mechanisms responsible of organizing the epithelial layers.

Recently, in our group it was described how a scale built using Voronoi diagrams (CVT, Centroidal Voronoi Tessellation (**Figure 8**)) was able to capture, at level of polygon distributions, any natural packed tissue arrangement (Sanchez-Gutierrez et al., 2016). The cited work explains how the tissues in which its cells maintain an equilibrium of forces, will be physically constrained, limiting and regulating its organization. The Voronoi

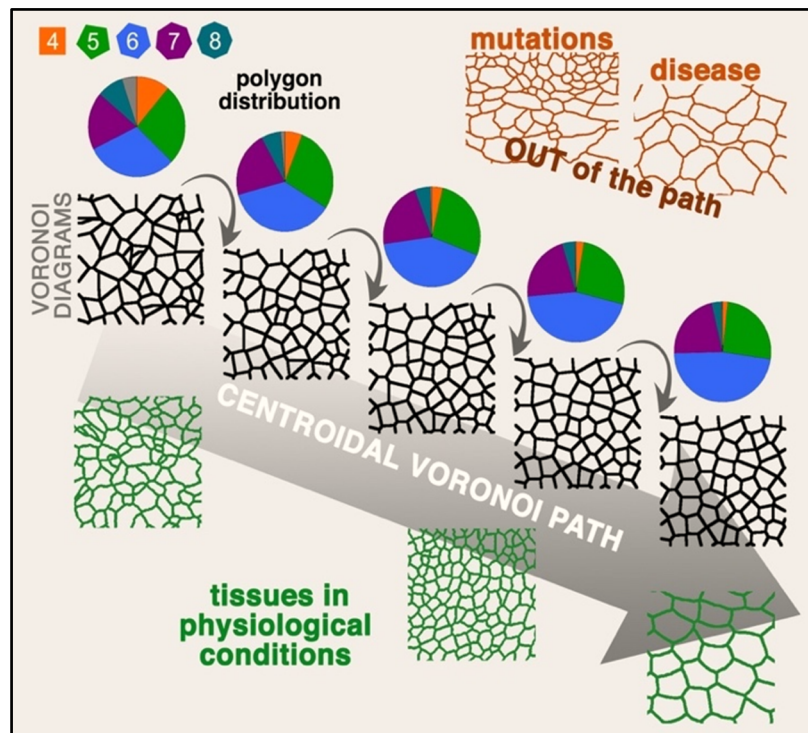


Figure 8. Centroidal Voronoi Tessellation (CVT) path

Biological packed tissues (green) could be found as patterns in nature with very different polygon distributions. These patterns can be reproduced by the Voronoi diagrams that conform to the Centroidal Voronoi Path (CVT, black). The CVT path is created by applying iteratively the Lloyd algorithm (Lloyd, 1982) beginning from a random Voronoi diagram (seeds randomly placed). Over Lloyd iterations, cells become increasingly homogeneous between them. It has been found that the packed tissues in physiological conditions arrange similarly than the CVT path diagrams in terms of polygons distributions. However, an unbalance of forces over a tissue, caused by any mutation or atrophy (orange) could break this rule, outlying from the CVT scale. Adapted from (Sanchez-Gutierrez et al., 2016).

diagrams, by definition, hold the same balance. In this way, it was unmasked a primary level of cell arrangement correlating with the tissue homogeneity.

The results suggested that the natural tissues in homeostasis could not be freely organized, being biophysically constrained. The *CVT* path was able to encompass the organization in stationary states of packed tissues just comparing its polygons distributions. Also, it is important to note that natural tissues in non-physiological conditions, for example in disease, could manifest forces unbalance that deviate the pathological tissue from the *CVT* path.

In summary, we consider that packed tissues share organization principles with the Voronoi tessellations and that they are under the same physical constrictions that drive its arrangement. We clear up that the Voronoi diagrams are a suitable tool to mimic and study the development of the natural tissues. The Voronoi tessellations together with the polygon distribution analysis shed us deterministic information about the rules prevailing in how the nature structures itself. Note that frequently the Voronoi diagrams are used as a source in vertex models. Lastly, the importance of using mathematical concepts to study the cell arrangements in the planar epithelial surface has paved the way for the following step: the analysis of the three-dimensional packing of epithelia.

1.6. The complexity of the three-dimensional packing in epithelia

Until now, the majority of the published researches about how epithelia organized has focused on the cellular arrangement over the apical surface (*2D*) of the epithelium. Likewise, the textbooks have traditionally described the epithelial cells as prisms with polygonal bases representing their apical and basal surfaces (Alberts et al., 2015; Gilbert and Barresi, 2013) (**Figure 9A-B**). However, it is demonstrated that coordinated changes of individual cells shapes along the morphogenesis induce complex tissue rearrangements to build the functional organ architecture. That is the case of the gastrulation process when the mesoderm bends himself or the formation of the neural tube in vertebrates where the cells tend to change its shape from prism to ‘frustum’ shape (Davidson and Davidson, 2012; Lecuit and Lenne, 2007; Pearl et al., 2017) (**Figure 9B**). A frustum is a variation of a prism in which, this geometrical figure adopts a shape like a truncated pyramid contained between two planar and polygonal bases (Schneider and Eberly, 2003). Hence, the bases have the same number of sides but differ in size, it is to say, that is enough knowing how organized the apical layer to understand the global *3D* architecture.

Certainly, it is required a more faithful approach than the idealization of the tissue “three-dimensionality” from 2D data, to extract and analyse the high amount of information enclosed in any morphogenetic process taking place along the three dimensions. So far, the three-dimensional study at the cellular level has been restricted to a reduced number of developmental procedures such as tissue invagination or tube formation, by analysing the apical surface of 3D structures (Monier et al., 2015; Osterfield et al., 2013) or by developing lateral vertex models (Fletcher et al., 2014; Štorgel et al., 2016). Even more specific, few of groups have tried to go beyond focusing their works on the comprehension of three-dimensional curved epithelia through the combination of 3D experimental data with powerful computational approaches and image analysis (Goodwin and Nelson, 2017; Khan et al., 2014; Kim et al., 2013).

Remarkably, all the cited works considered the cells, afresh, as frusta or prisms. Nevertheless, it exists previous evidences of epithelial cells changing their contacted-cells along the apico-basal axis of the epithelial layer. This feature is not compatible with the assumption of the cells having a frustum or prism shape. The emergence of this event, with the difference of the space replacing the time dimension, has been observed in imaginal discs of *Drosophila* (Condic et al., 1991), in the development of the Wolffian duct epithelium in mouse (Xu et al., 2016), in the course of the *Drosophila* germ-band extension (Sun et al., 2017), in the *Drosophila* embryo cellularization (Rupprecht et al., 2017) and during the development of the *Drosophila* salivary glands placode (Sanchez-Corrales et al., 2018). Moreover, a computational model reflected that phenomenon in a framework where it is simulated a monolayer tissue during a process of elongation (Honda et al., 2008). Interestingly, the apico-basal exchange of neighbours presents a comparable situation with the cell rearrangement along the time as a consequence of cell migration or reallocation during the development. This is what is known as *T1* transition of a four-cells motif (**Figure 9C**). When we refer to this occurrence along this document, we have named it as spatial *T1* transition, apico-basal cell intercalation or apico-basal transition.

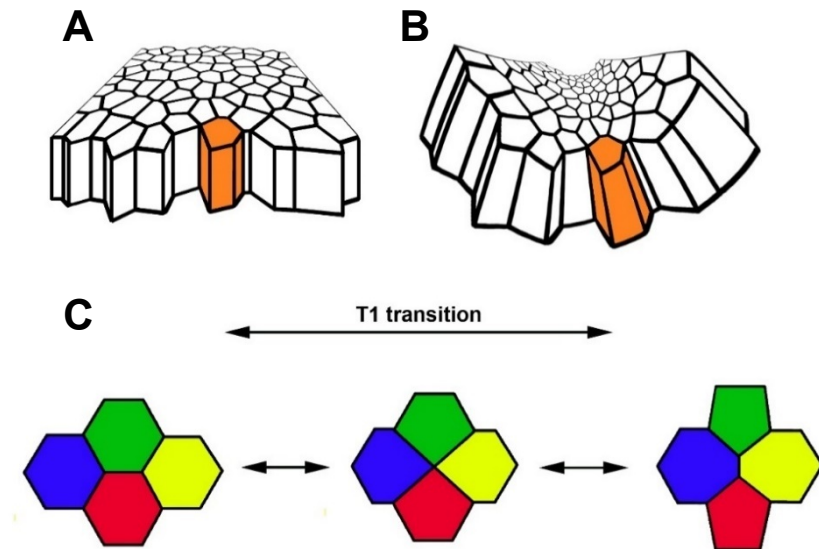


Figure 9. Epithelial 3D shapes and T1 transition

A) Simplification of a 3D planar epithelium where all the cells are prisms. **B)** Folding tissue where all the cells are frusta. **C)** Scheme of 4 cells involved in a T1 transition. Along a T1 the cells exchange its neighbours after touching all of them in a point.

OBJECTIVES

The cornerstone that guides our investigation is the understanding of how tissues are organized in homeostasis as a key factor to uncover the mechanisms of developmental processes. This work is focused on unmasking the properties behind the three-dimensional packing in epithelia. The principal objectives are structured as follow:

1. Develop a *3D* computational model using the Voronoi principles to mimic the tissue architecture in curved epithelia, providing a realistic three-dimensional framework to unveil the key factors managing the epithelial organization.
2. Analyse the three-dimensional epithelial organization in different organs and model organisms using cutting-edge image processing techniques applied to confocal stack images representing *3D* sections of epithelial tissue.
3. Apply the cited image processing methodology to explore how different tissue curvatures affect epithelial arrangements.
4. Uncover the biophysical fundamentals that regulate the cellular organization to reach the final *3D* epithelial conformation taking advantage of computational tools.

MATERIALS AND METHODS

3.1. Conceptualization of Voronoi diagrams on parallel curved surfaces

At the beginning of this project, our group established a collaboration with the mathematicians, Dr Alberto Márquez (Universidad de Sevilla, Seville) and Dr Clara Grima (Universidad de Sevilla, Seville) to study how to generate Voronoi diagrams on curved surfaces (Grima and Márquez, 2001). They indicated us that Voronoi diagrams must be constrained to occupy a defined curved surface just considering some key factors: the Voronoi seeds, the dimensional space and the metric, with the final aim of modelling an actual curved tissue. If we consider every Voronoi region as R_n , and P_n its point generator (the seed) that is contained in a surface S , then both R_n and $P_n(u, v) \in S$. From $P_n(u, v)$ emerges a vector $N(u, v)$ with L length, that is orthogonal to the tangent plane to S in $P_n(u, v)$. Therefore, we found that is possible generating a Voronoi diagram in any new parallel surface (S_α) between $[0, L]$. Thus, each P_n should have its equivalent in S_α , that is defined by

$$P_\alpha = P_n(u, v) + \alpha N(u, v), \text{ where } \alpha \in [0, 1]$$

Additionally, each Voronoi diagram generated from the set of superficial seeds P_α covering the parallel surfaces must follow a geodesic metric. In other words, the distance between two coordinates placed over the same surface is delimited by its geodesic distance, and it is a key rule in the Voronoi diagram construction.

In this way, the method of simulating curved natural tissues begins placing a set of seeds (P_n) located in the initial surface (apical in nature). From each seed emerges a segment up to the outer parallel surface (basal in nature), and the interception of these segments with any parallel surface (S_α) will determine the seeds of the Voronoi diagram on the intercepted surface. Therefore, if we compute the Voronoi diagram of every parallel surface and then connect all the surfaces, we reach a three-dimensional structure as a compendium of different spatial layers between basal and apical. Consequently, each 3D Voronoi cell depends on the different 'parallel Voronoi regions' developed from the seeds parallelly located along its specific segment. Thus, from a segment we could obtain a 3D Voronoi cell.

3.2. Computational models

All the computational experiments were carried out using the software Matlab 2014b (Mathworks). The full code is accessible at (<https://github.com/ComplexOrganizationOfLivingMatter/Epithelia3D/tree/master/InSilicoModels/paperCode>) under GPLv3 license.

3.2.1. Voronoi tubular model

We have developed a computational model attempting to imitate a tubular epithelium. This model was constituted by an inner and an outer surface, mimicking the biological apical and basal layers. These *in silico* cells layers were built based on the Voronoi rules. A previous work of our research group described the centroidal Voronoi tessellation path (CVT) as a benchmark to capture the organization of biological packed tissues over the 2D space (Sanchez-Gutierrez et al., 2016). This study was taken as a reference to develop this model over a cylindrical shape. The full pipeline is detailed as follows:

1. We developed the inner cylindrical surface into a 2D Euclidean plane with dimensions 512×4096 pixels (**Figure 12B**).
2. A set of seeds were randomly placed over there. We did several samplings, using 40, 80, 200, 400 and 800 seeds, for 20 different realizations.
3. The initial image containing the selected set of seeds was tripled along the X axis (transverse axis of the cylinder), getting a 1536×4096 pixels image, together with the set of seeds tripled.
4. Once the workspace is tripled, applied the Voronoi algorithm building the Voronoi cells that filled the layer.
5. The centroid of each Voronoi cell placed in the central region (delimited by the pixels 513 and 1024 of the X axis, and the full Y axis) was calculated and stored to be used on following steps.
6. Then, the cited central region was cropped getting again a 512×4096 pixels image, like the initial one. This crop allowed that cells contacting with a border of the X axis (pixels 1 or 512) to be continuous in the other extreme when we obtain the image as a tube.

This procedure explained how to make a Voronoi tube using a bidimensional metric. Then, this protocol (from 3 to 6) was repeated (4 times) using the centroids of the Voronoi region as new seeds, that is, developing Lloyd's algorithm over a tube. Therefore, for each one of the 20 different random initial images, we reached 5 different Voronoi. The final Voronoi diagram is what we called a Voronoi diagram 5, that looks like a

homogeneous cell distribution widely observed in nature (Gibson et al., 2006). This diagram would be the inner layer of the tube and the starting point to build the outer cylindrical layers, extending the transverse axis and keeping constant the longitudinal axis of the tube.

For each one of the inner tubes, we developed 10 expansions, in which the radius of the external tube increased considering this formula: $R_{basal} = R_{apical} \cdot SR$, where SR (surface ratio) stood from 1 until 10 following this formula, $SR(x) = \frac{1}{1-\frac{x}{10}}$ considering $x \in \mathbb{N}, \forall x$ where $0 \leq x \leq 9$. Once we built the concentric outer tubes, we constructed the Voronoi diagrams over there by using the extrapolation of the Voronoi seeds located in the inner tube (**Figure 10A-C**). If we treat this conceptualization from the 2D perspective, to build the Voronoi diagram over the new expanded image, we resized the X axis by multiplying each SR by the apical axis length. In the same way, we multiplied the X coordinate of the apical seeds by the SR to reach the new seeds location for each outer layer. Then, we applied the described 3, 4 and 6 steps to the enlarged images embodying the outer cylindrical Voronoi diagrams.

A Voronoi cell that emerged from an apical seed or its external extrapolation would be tagged with the same label in all the cylindrical surfaces, being layers of a whole 3D Voronoi cell (**Figure 12A-B**).

3.2.2. Voronoi tubular model measurements

This model was used to carry out some measurements, such as the length and angle of the cellular outlines for the apical and all the expanded basal surfaces (**Figure 14A**). The angular reference (0°) matched with the transverse axis (X axis in 2D). Besides these geometrical measurements, it was recorded the basal intercellular edges of 4-cells motifs participating in apico-basal cell intercalations, obtaining the proportion of scutoidal cells (a cell participating in an apico-basal transition is an scutoid). The cells contacting with a border tip in any of the layers were considered non-valid cells. The measurements where this type of cells was involved, were discarded.

These data were represented using 200 random measurements over polar scatter plots (edge length VS angle), and dividing this information into two graphics: promoting and non-promoting apico-basal transitions (**Figure 14C-F**).

Conjointly, it was quantified some measurements required to feed the "line-tension minimization model". They were geometrical measurements related to the aspect ratio for each 4-cells motif and its intercellular shared edge: the sum of outlines length into the

packing configuration (L_T), together with the width (w) and height (h) (**Figure 21A**). A random set of 100 quantifications was used to display the energy trajectories of cellular motifs from the basal to the apical surface, differentiating the cases of apico-basal transitions and the motifs without cell intercalations (**Figure 22B**). We only considered the intercellular shared edges larger than 4 pixels, in order to avoid inconsistencies or artefacts (i.e. finding an edge where could exist a fourfold vertex) in any of the layers. This tolerance value was chosen after analysing a spherical Voronoi where scutoids should not appear (**discussion**). However, scutoids emerged in some cases when we analysed edges smaller than 4 pixels. Therefore, we applied the cited threshold to all our models.

3.2.3. Voronoi spheroidal model

The spheroidal model was implemented motivated by the study of the cell organization when the three axes of curvature are non-null. In this way, we simulated the structural characteristics of *Drosophila* egg chamber at stage 4 (130 randomizations: X radius inner layer = 1.26, $cell_{height} = 0.22$, $N = 200$) and 8 (30 randomizations: X radius inner layer = 2.16, $cell_{height} = 0.15$, $N = 450$) during the development, imitating the apical axial radii, the cell density (N) and its average height ($cell_{height}$), considering the Y and Z apical radii as a unitary reference (**Figure 20A-B**). Each unit represents 100 pixels in the model workspace, i.e., if Y radius = 1, then Y radius = 100 pixels.

In addition, we developed a sampling of different spheroidal models, modifying the radii of curvatures to explore the consequences of this change of curvature in terms of cell packing: We fixed the ellipsoid axial radii along the Y and Z axes (unitary reference), modifying only the X axial radius. The X radius took the values 1 embodying a “Sphere”, 1.5 getting a “Globe-like” shape and 2 representing a “Zeppelin” (**Figure 19A-C**). A set of 10 realizations were created for each of these structures, providing 3 different basal layers after inferring 3 cell heights: 0.5, 1 and 2. The methodology used to build the Voronoi spheroids is explained below:

1. We tried to create a spheroid tessellation, with N cells, approximately homogeneous between them in terms of size like occurs in nature. With this purpose, we delimited a minimum distance between the possible positions of the Voronoi seeds over the apical surface (depending on the surface area). In some cases, this constriction did not allow the exact presence of N cells over the surface due to lack of surface space, reducing this number in some units.
2. Once the apical seeds were located over the apical layer, we extrapolated them to the basal surface using the ellipsoid equation:

$$\frac{x^2}{a^2} + \frac{y^2}{b^2} + \frac{z^2}{c^2} = 1$$

where, x, y and z represent the X, Y and Z coordinates of a point over the ellipsoid surface, and the parameters a, b and c correspond to the 3 axial radii of the spheroid (X, Y and Z respectively).

3. Finally, we developed the Voronoi algorithm over each surface.

3.2.4. Voronoi spheroidal model measurements

The measurements carried out over the Voronoi spheroidal model were very similar to the properties evaluated in tubular models. The method used to extract these features was adapted to get the measurements from 2D projections of the models, in the same way than we did for the confocal images of *Drosophila* egg chambers (**methods, egg chambers measurements**). Consequently, if a layer of our 3D Voronoi spheroidal models have the dimensions $[-X_{radius}, X_{radius}; -Y_{radius}, Y_{radius}; -Z_{radius}, Z_{radius}]$ being the origin of coordinates (0,0,0) the geometric centre of the spheroid, we obtained four 2D projections from each one of these layers: two of them along the Z_{axis} (First from $Z = -Z_{radius}$ to $Z = 0$; Second from $Z = Z_{radius}$ to $Z = 0$), and the two others along the Y_{axis} using the same methodology. Subsequently, we selected a *ROI* into each projection trying to reproduce the protocol followed to analyse the *Drosophila* egg chambers. These *ROIs* only selected valid cells (without touching the borders) and approximately was delimited by 2 X_{axis} bounds: $X \in \left[-\frac{2}{3} \cdot X_{radius}, \frac{2}{3} \cdot X_{radius}\right]$, trying to capture the central region of each projection.

Once all the spheroid layers were projected, we chose the 4-cells motifs composed by valid cells, and measured the same properties than in tubes: the intercellular edge length and angle (regarding the transverse axis), percentage of scutoids (**Table 3**), L_T , w and h (**Figure 21A**). As mentioned in tubes, here it was applied the threshold of 4 pixels to consider the quantifications of an intercellular edge. A total of 100 cases of transitions and a further similar of non-transitions samples were randomly taken to represent the energetic trajectories from the outer to the inner surfaces (**Figure 23A**). Similarly, 200 samples for each condition were used to plot the polar scatters (edge length VS angle) (**Figure 20C-D**).

Finally, we measured the two principal curvatures (k_1 and k_2) for each voxel considered in the region of interest of inner and outer 3D layers: $\forall X$ where $X \in \left[-\frac{2}{3} \cdot X_{radius}, \frac{2}{3} \cdot X_{radius}\right]$, being the remaining axes fully explored. k_1 and k_2 values were calculated by following the formulas of (Bektas, 2017). Then, we computed the average

value regarding the maximum (k_1) and minimum (k_2) radii of curvature ($R = \frac{1}{k}$) of the voxels (both in apical and basal). These measurements provided us the value of the parameters R_b^h, R_b^w, R_a^h and R_a^w . h , stands for the axis of greatest curvature (i.e. transversal axis in Voronoi tube), w , for the axis of least curvature (longitudinal axis in Voronoi tube), being a the apical surface and b the basal one. Therefore, $R^w = \frac{1}{k_1}$ and $R^h = \frac{1}{k_2}$. As R refers to the Cauchy radius, then R_a^w is the average Cauchy radius along the apical surface by considering the longitudinal axis (w).

With these parameters, we have built a general model in which we directly correlated the proportion of scutoids with the surface ratio anisotropy $\left(\frac{R_b^h}{R_a^h} / \frac{R_b^w}{R_a^w} - 1\right)$ of the Voronoi model (**Figure 24**).

3.3. Biological models

3.3.1. Immunohistochemistry and confocal imaging

The tissues staining and imaging in the case of the *Drosophila* salivary glands were developed from our members of the wet lab (Antonio Tagua, Ana M. Castro and Marta Letrán). On the other hand, our collaborators supported us with images from other biological tissues: Dr Sol Sotillos (CABD, CSIC/JA/UPO, Campus Universidad Pablo Olavide, Seville) provided us with *Drosophila* embryos images; Dr María D. Martín-Bermudo (CABD, CSIC/JA/UPO, Campus Universidad Pablo Olavide, Seville) and Dr Andrea Valencia-Expósito (CABD, CSIC/JA/UPO, Campus Universidad Pablo Olavide, Seville) sent us *Drosophila* egg chambers images at different development stages and Dr Florencia Cavodeassi (Centro de Biología Molecular Severo Ochoa and CIBER de enfermedades raras, Madrid. St. George's University of London, London) supplied Zebrafish embryos images. All these images were obtained as described the methods of the original paper (Gómez-Gálvez et al., 2018), and then, were computationally processed to be analysed.

3.3.2. Topological quantifications

Drosophila salivary glands

Taking on the shape of the glands resembling a tube, some parameters were measured over the confocal images after identifying all the local 4-cells motifs, where at least two of these cells were placed on the central region. A central cell is a cell whose basal and apical surfaces are completely visible in a single confocal slice, while for a

lateral cell it was necessary a multi-sliced confocal reconstruction to capture either basal or apical surfaces.

Then, after locating the cellular motifs, we measured distances and angles of the cells outlines (only basal and apical surfaces) directly on the confocal stacks (**Figure 14A**) using the *Straight Line* tool in FIJI (Schindelin et al., 2012). These parameters were:

- Intercellular edge length.
- Intercellular edge angle regarding the transverse axis (0° reference).
- L_T , w and h as in the *in-silico* models to feed the energetic model (**Figure 21A**).
- Surface ratio ($\frac{R_b}{R_a}$) of salivary gland. Measuring the gland and lumen diameter ($2 \cdot R_b$ and $2 \cdot R_a$ respectively) at the confocal slice where the lumen was completely visible.

Besides the percentage of scutoidal cells, i.e. the percentage of cells participating at least in one apico-basal transition.

Drosophila embryo

The confocal images stacks of *Drosophila* embryo (gastrulation stage) could be differentiated on 2 different local regions of interest (*ROI*): the folds and the flatter zones (**Figure 16A-B**). In the selected *ROIs*, we measured the percentage of scutoids, the surface ratio (cell area in larger surface / cell area in smaller surface), the intercellular edge length and angle (regarding the transverse axis of the folds) for 10 four-cells motifs with and without apico-basal transition (per stack).

Drosophila egg chambers

To carry out some quantifications on the confocal stacks of the *Drosophila* egg chamber, the central region of each sample was selected by including the follicular cells which were considered as central cells. As in salivary glands, a central cell is the cell whose basal or apical surface could be visualized just looking a unique confocal slice. These central cells were captured on a *ROI* where it was measured the percentage of scutoids, the edge length and angle (regarding the transverse axis (Y)) of the four-cells motifs, and the parameters needed to feed the line-tension minimization model using the same FIJI methods than in salivary glands.

Additionally, we registered the axes dimensions of the egg chambers at different development stages, and the average height of the cells.

Zebrafish embryo

We simplified the measurements isolating this multilayer embryo at 50% of epiboly to the two more superficial layers and selected 10 cellular-motifs with apico-basal transitions and 10 without it. Then, we chose again the central motifs (same criteria than salivary glands and egg chambers) and measured the length and angle (regarding the *X*-axis) of the intercellular edges. Additionally, it was quantified the number of cells and the percentage of scutoids in these two layers.

3.4. Biophysical model – line tension minimization model

The protocol followed to biophysically analyse the presence of scutoids was implemented by our collaborator, the physicist Dr Javier Buceta (Lehigh University, Bethlehem, USA). The pipeline can be visited on the methods of the original paper (Gómez-Gálvez et al., 2018).

3.5. Statistics and illustrations

Kolmogorov – Smirnov statistical analysis

We developed the two-sample test: *Kolmogorov – Smirnov* to test if two different samples had the same continuous distribution (**Table 1**). We analysed specifically the edge angles and lengths distributions represented in the polar scatter graphs (**Figure 14B-F, Figure 16D, Figure 17D, Figure 18C, Figure 20C-D**), and compared the transitional and non-transitional cell edges (intercellular edges of 4-cells motifs involved or not in apico-basal transitions). This analysis was computed by using the *kstest2* function of *Matlab*.

3D segmentation of *Drosophila* larval salivary glands

We implemented a pipeline to segment, label and track every individual cell along the confocal planes of salivary glands (**Figure 11A**). The protocol followed these sequential steps:

1. Using *Trainable Weka Segmentation* (Arganda-Carreras et al., 2017), a FIJI plugin to segment images based on machine learning classification. We marked some cells outlines of a representative confocal slice with a colour label and the background with another to feed and train the classification model. This model was applied to every slice of the confocal stack images getting as output a binary segmentation of the cells outlines (cell outlines = 1, background and cell body = 0).

2. Manual curation using *Adobe Photoshop CS6*. Correcting mistakes of the cell automatic segmentation, including the salivary gland lumen detection.
3. Image processing using *Matlab 2014b*. We developed a script to numerically tag the segmented cells and track them along the Z-stack by comparison of areas and centroids, in addition to homogenizing the width of cells outlines (1 pixel). However, it was necessary a manual inspection to corroborate the accurate cells tracking. Finally, we got a series of segmented confocal planes of salivary where its cells were labelled with numbered identifiers and colours (**Figure 11A**).

3D reconstruction

Using the computational Voronoi tubular model, we carried out the 3D reconstruction of a four-cells motif immerses in an apico-basal transition (**Figure 10G**). We took as source the different surfaces from $SR = 1$ until $SR = 2.5$ and inferred the interplanar space using the *AlphaShape* Matlab function, getting the 3D bodies of the cells. Additionally, to represent each surface, we have taken the planar Voronoi diagrams (**Figure 12B**) and applied the *Wrap* Matlab function obtaining rolled surfaces that would compose the lateral surface of a cylinder (**Figure 12A**).

Regarding the salivary glands, the same protocol than in Voronoi tubes was applied to reconstruct a four-cells motif promoting apico-basal cells intercalations. Here, we took advantage from the segmentation along the confocal Z-stacks, and applied the same *AlphaShape* function to get the structure of this group of cells along the three-dimensions (**Figure 11A**).

The spheroids 3D representations were computed by using initial seeds segments joining the seeds of the apical and the basal surfaces. In the same way, each of the spheroid cells was reconstructed with the *AlphaShape* function (**Figure 19A-C**, **Figure 20A-B**).

RESULTS

4.1. A Voronoi tubular model unveils cells exchanging its neighbours along the apico-basal axis.

Traditionally, the epithelial cell shape has been assumed as a prism in non-curved tissues (**Figure 9A**) or adopting a frustum shape when the curvature appears (**Figure 9B**). With the aim of analysing how the epithelia organize in 3D curved geometries, we designed a computational model following some assumptions related to the Voronoi tessellations (**methods**). Specifically, the target of this model was studying the epithelial packing within tubular structures (**Figure 10A-C, methods**). Our model was composed of two concentric tubular surfaces, defined by two cylindrical radii: R_a , for the inner tube imitating the apical surface of the epithelium and, R_b , for the outer simulating the basal side. Both measurements define a surface ratio (SR), by the relation $SR = \frac{R_b}{R_a}$.

To build the tubular models, we started from a set of seeds placed over the apical surface, and from them emerged the Voronoi cells filling this layer (**Figure 10A**). In a second step, these seeds were extrapolated to the basal surface (**Figure 10B**) and generated a new Voronoi diagram in the basal layer (**Figure 10C**).

In some cases, we observed a change in the topology between the two surfaces: the cells had different neighbours in each one of the surfaces (**Figure 10D**). This occurrence was due to a differential enlargement between the transversal and the longitudinal axes of the cylinders. If we look carefully to the seeds displacement from the apical to the basal surface, its positions are constant along the longitudinal axis, but the seeds move away along the transversal axis (**Figure 10B**, blue and yellow cells). This implies that, in the tubular model, neighbouring cells were exchanging their contacted cells in a similar way than happen in the well-known *T1* transitions on diverse morphogenetic events, leading temporal cell intercalations (in 2D) (Bertet et al., 2004; Lecuit and Wieschaus, 2002; Zallen and Zallen, 2004) (**Figure 9C**). The difference was that, in our model, the intercalation occurred spatially, along the apico-basal cell axis (**Figure 10D**).

That result was incompatible with the traditional assumption of prismatic or frustum-like cells (**Figure 9A-B**) filling the three-dimensional tissues. Thus, we unveiled a new paradigm that explains how 4-cells motifs could intercalate their neighbouring cells along the 3-dimensions, producing a novel geometrical shape (**Figure 10E**). This geometrical entity owns the following characteristics:

- It contains at least a vertex along the apico-basal axis. One vertex for each apico-basal cell intercalation (or spatial change of neighbours) (**Figure 9C** and **Figure 10D-E**).
- It can present a mix of concave and convex surfaces (**Figure 10E**).

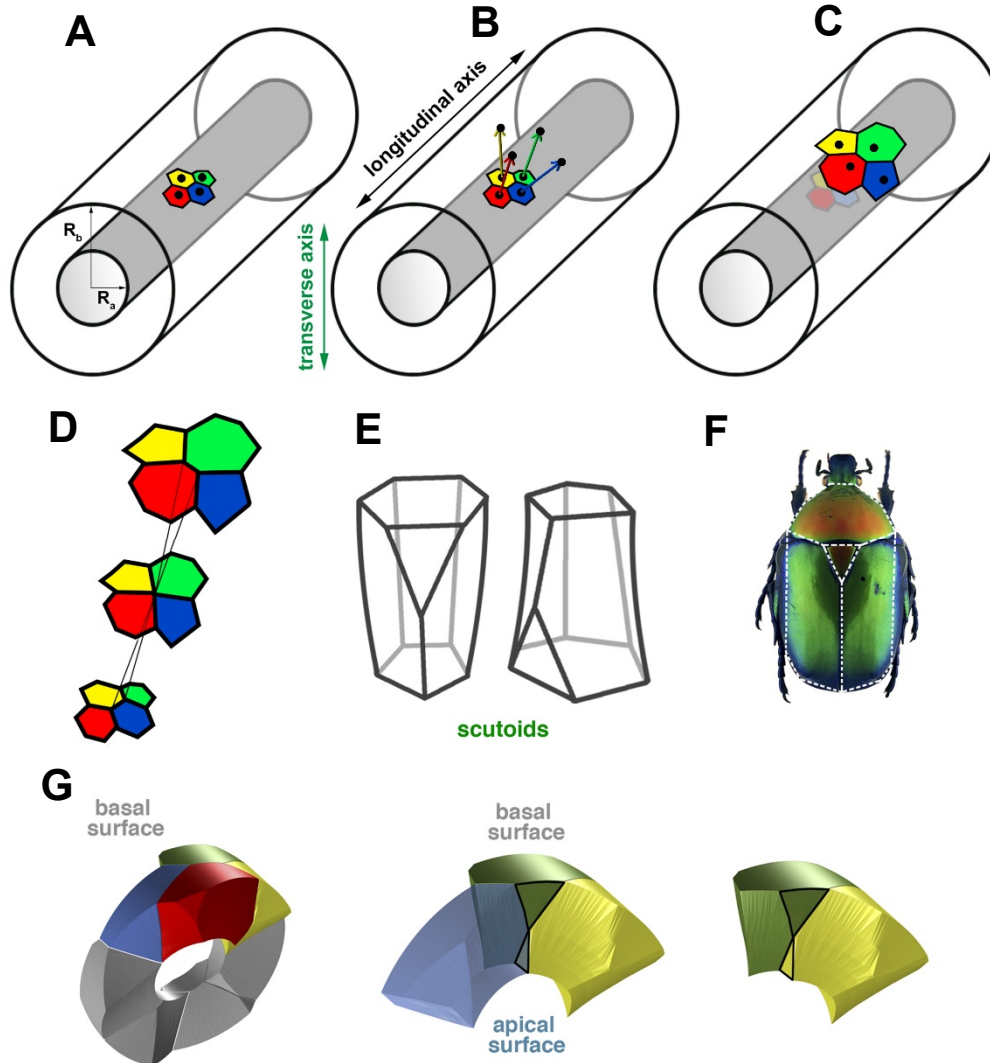


Figure 10. Voronoi tubular model

A) The tubular model composed by an inner tube defined by the R_a radius and a concentric outer tube defined by the R_b radius. Over the inner tube a set of Voronoi cells have emerged from a set of seeds. **B)** The same inner seeds are extrapolated to the external surface. **C)** The Voronoi diagram is constructed using the metric of the cited surface. **D)** Four-cells motif exchanging its neighbours along the apico-basal axis. **E)** Schematic 3D solid obtained from the tubular model. **F)** *Protactia speciose* beetle of the Cetoniidae family, from (Gómez-Gálvez et al., 2018). **G)** 3D reconstruction of simulated cells along a transversal section of the Voronoi tubular model, with $SR = 2.5$. The coloured cells participate in the apico-basal cell intercalation, showing how the blue and yellow cells are contacting in apical, but not in basal, and just the opposite occurs for the green and red ones.

Since this type of solid has not ever been described (to our knowledge), we coined it with the term ‘scutoid’. This name was assigned due to the resemblance of a lateral view of the solid (**Figure 10E**) with the scutum/scutellum topology in the thorax of some beetles’ subfamilies (**Figure 10F**).

Using the Voronoi tubular model we were able to build the 3D cells. We assembled the apical and basal surfaces of each cell by interpolating some intermediate layers with them until getting a 3D solid (**methods**). Thereby, we three-dimensionally reconstructed some Voronoi cells immersed in an apico-basal transition (**Figure 10G**). From this representation, it was verified how scutoids got concave and curved surfaces and had at least a vertex placed in an intermediate plane between the apical and the basal surfaces.

4.2. Analysing the scutoids presence in epithelial tubes

Our computational model predicted a novel cell morphology just applying the Voronoi rules to tubular surfaces (**methods**), then we investigated if the biological tubular epithelia followed these same organizational principles. In this case, we examined the salivary glands of third instar *Drosophila* larva that exhibits a tubular structure, with an inner lumen covered by epithelial cells (**Figure 2, glandular**).

To fully explore the salivary glands at cellular level, we developed a computational pipeline to segment and track the cells along the whole volumetric glandular space, from Z-stacks of confocal images as source (**Figure 11A, methods**). The 3D image reconstruction of several segmented 4-cells motifs identified apico-basal cell intercalations, confirming the presence of scutoids on real epithelia (**Figure 11B**).

At this moment, our results suggested that the Voronoi tubular model was able to mimic the salivary gland packing (or vice-versa). To further deep down, we extracted some measurements to investigate the causes of scutoid prevalence (**methods**). First, we measured the percentage of scutoids ($75 \pm 17\%$, $SR = 7 \pm 3$) over a set of 40 *WT* glands, and 716 cells.

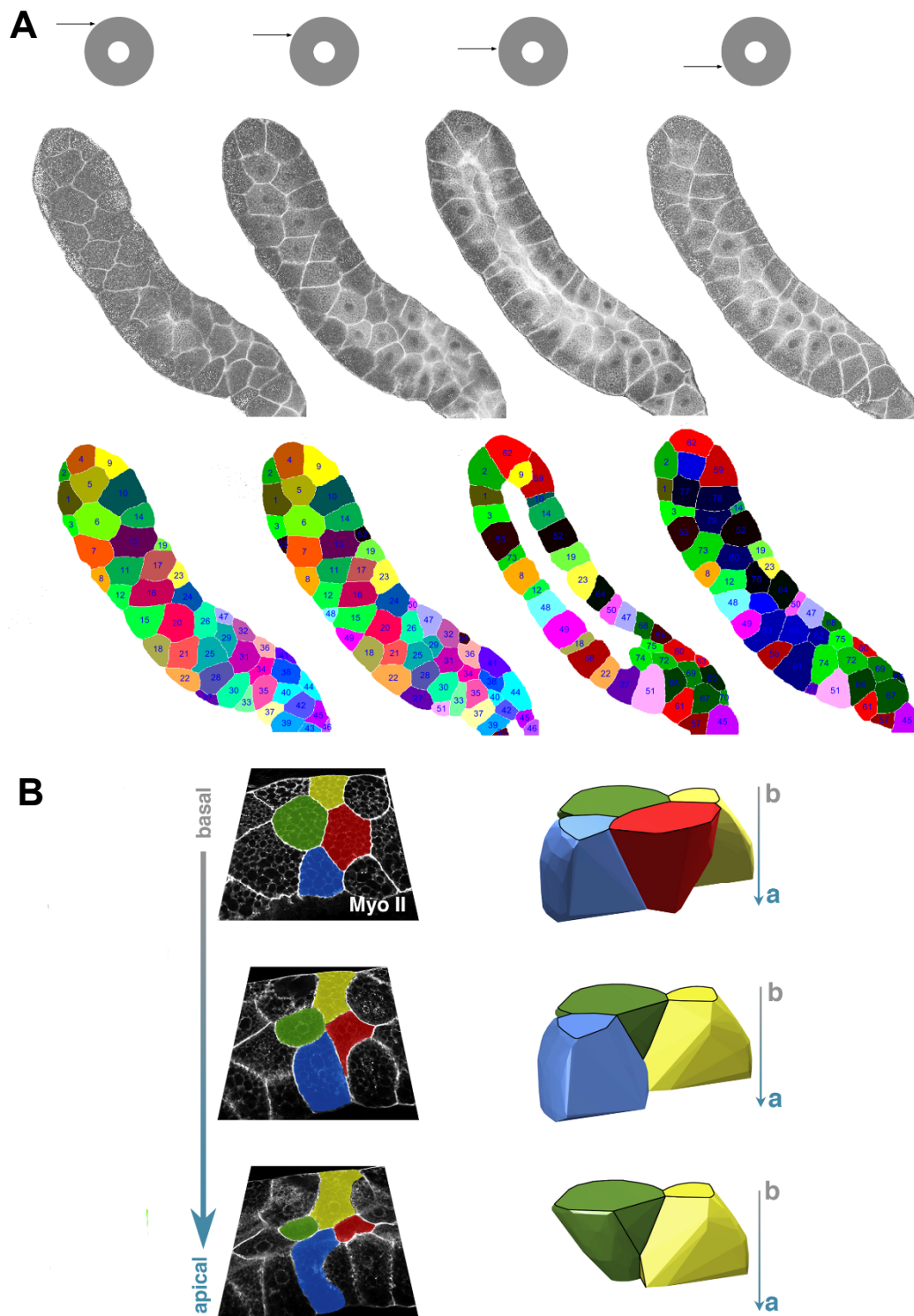


Figure 11. Tracking salivary gland confocal stacks

A) The top row represents the different Z depths where the confocal images showed below were taken. Each depth is marked by the arrows that point to the tubes above each image. The middle row is the confocal images of *Drosophila* salivary gland where its background has been deleted. The bottom row shows the segmented and tracked cells of the confocal images.

B) Scutoids/apico-basal cells intercalations detected from cells glands reconstruction (methods).

We repeated the measurements developed in salivary glands for the Voronoi tubular model. Specifically, we started with a diagram Voronoi 5 in the apical tubular surface (**methods**), because commonly share organizational traits with several observed epithelial arrangements in terms of polygons distributions (Gibson et al., 2006; Sanchez-Gutierrez et al., 2016). Once the apical surface was stated, we performed a set of basal expansions defined by the series of $SR: \frac{10}{10} (1), \frac{10}{9}, \frac{10}{8} (1.25), \dots$ until $\frac{10}{1} (10)$, and did a screening with different cell densities over the same superficial size (**Figure 12A-B, methods**).

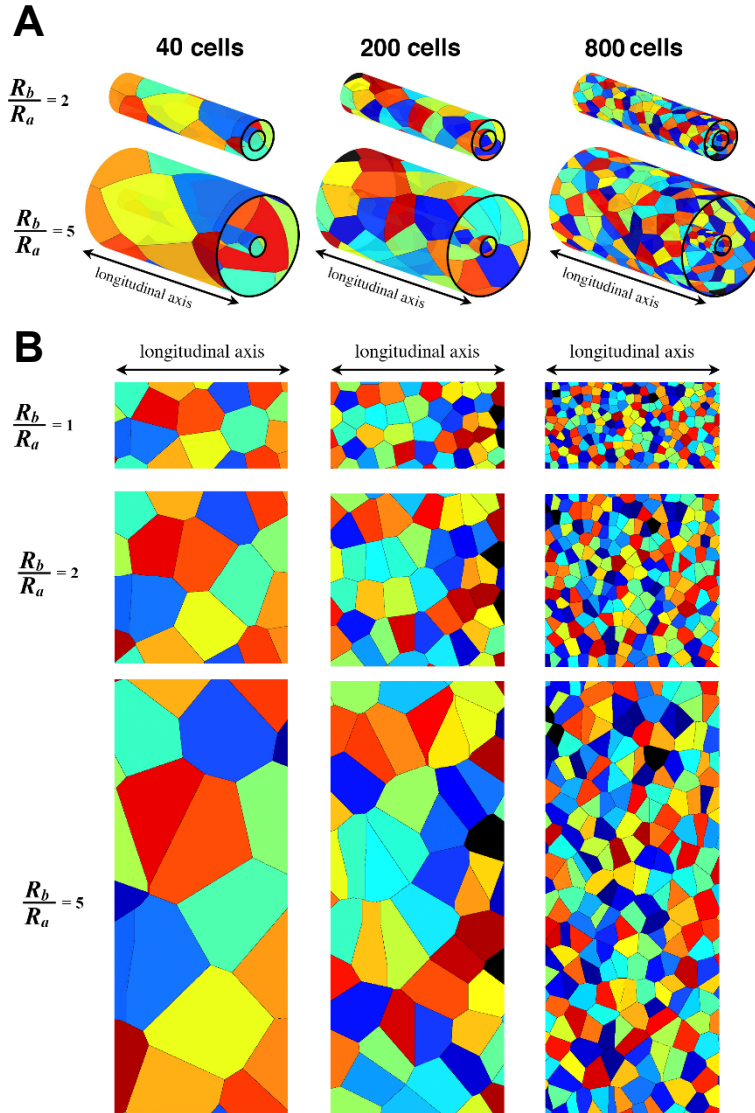


Figure 12. Voronoi tubular model screening

A) Modelling of cylindrical Voronoi surfaces using different cells densities (at the top) applied to some surfaces ratios expansions (at left: $\frac{R_b}{R_a}$). **B)** Developed surfaces of the Voronoi tubular models represented in **A**. The protocol to create the full model and take quantifications made use of these unrolled 2D cylinders (**methods**). These representations only consider $\frac{1}{4}$ of the real tubular length (**methods**).

Once these tubes were created, we quantified the percentage of scutoids among their total number of cells. We observed that the larger the SR value, the higher the percentage of scutoids. The 100% of scutoidal cells was reached in all the different simulations at a SR value of $\frac{10}{3}$ ($3.33\hat{3}$) (**Figure 13A**). Despite the percentage of scutoids could not overcome the 100%, we checked the average number of apico-basal cell intercalations along the different SR , where we observed a continuous increment of spatial transitions without apparent changing of tendency (**Figure 13B**). Additionally, it is showed how the change of cell density (40, 80, 200, 400 and 800 cells), in both cases, have no effect over the calculations. Nevertheless, we can observe how the tube with 40 cells deviates from the rest of samples due to the border effect. This factor disqualified the cells that in

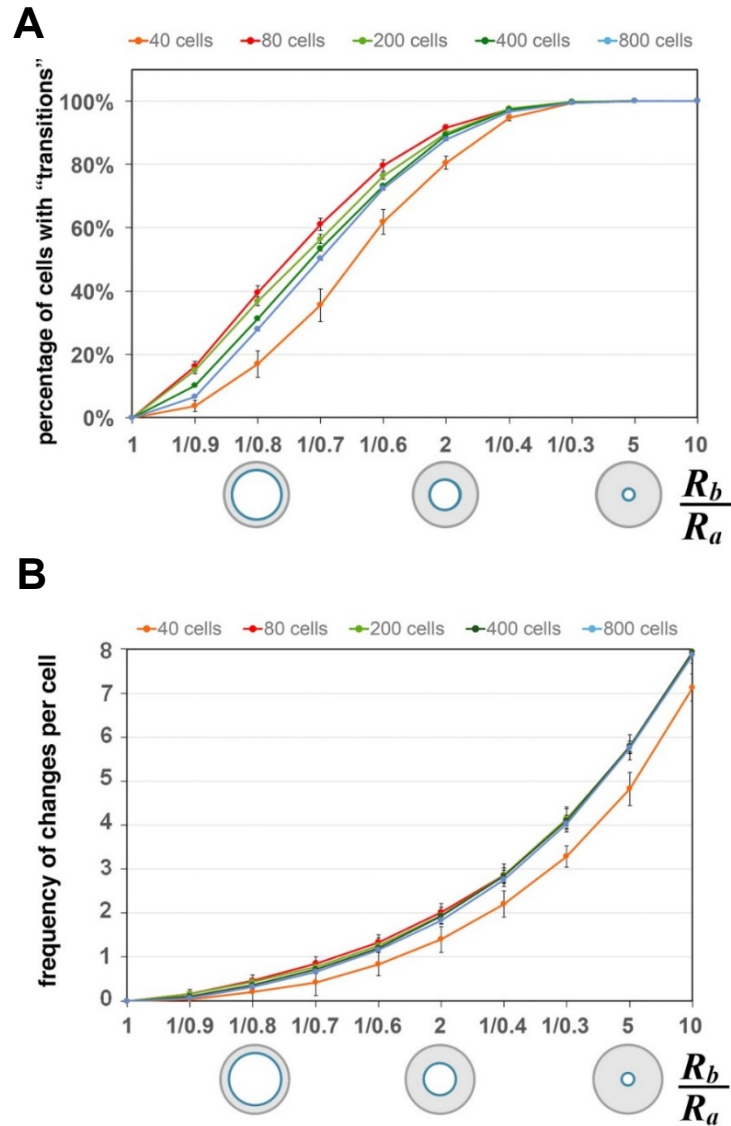


Figure 13. Quantification of neighbours exchanges

A) Percentage of total cells involved at least in an apico-basal transition (scutoidal cells) measured at different surfaces ratios with five cell densities (800, 400, 200, 80 and 40 cells, **methods**). **B)** Total neighbour exchanges at the same surface ratios and cell densities.

some moment could be in touch with the limits of the tube (border of the basis) and greatly restricted the number of possible scutoids or apico-basal intercalations. Therefore, this limitation vanished with the increase in the number of cells.

In a second step, we studied the geometrical implications of the cellular boundaries (length and angle) as indicators of scutoids appearance, both in glands and Voronoi tubes with a density of 200 cells. First, we checked the 4-cells motifs (802 in 40 glands) sharing an intercellular edge and measured: i) the value of the edge in the basal layer

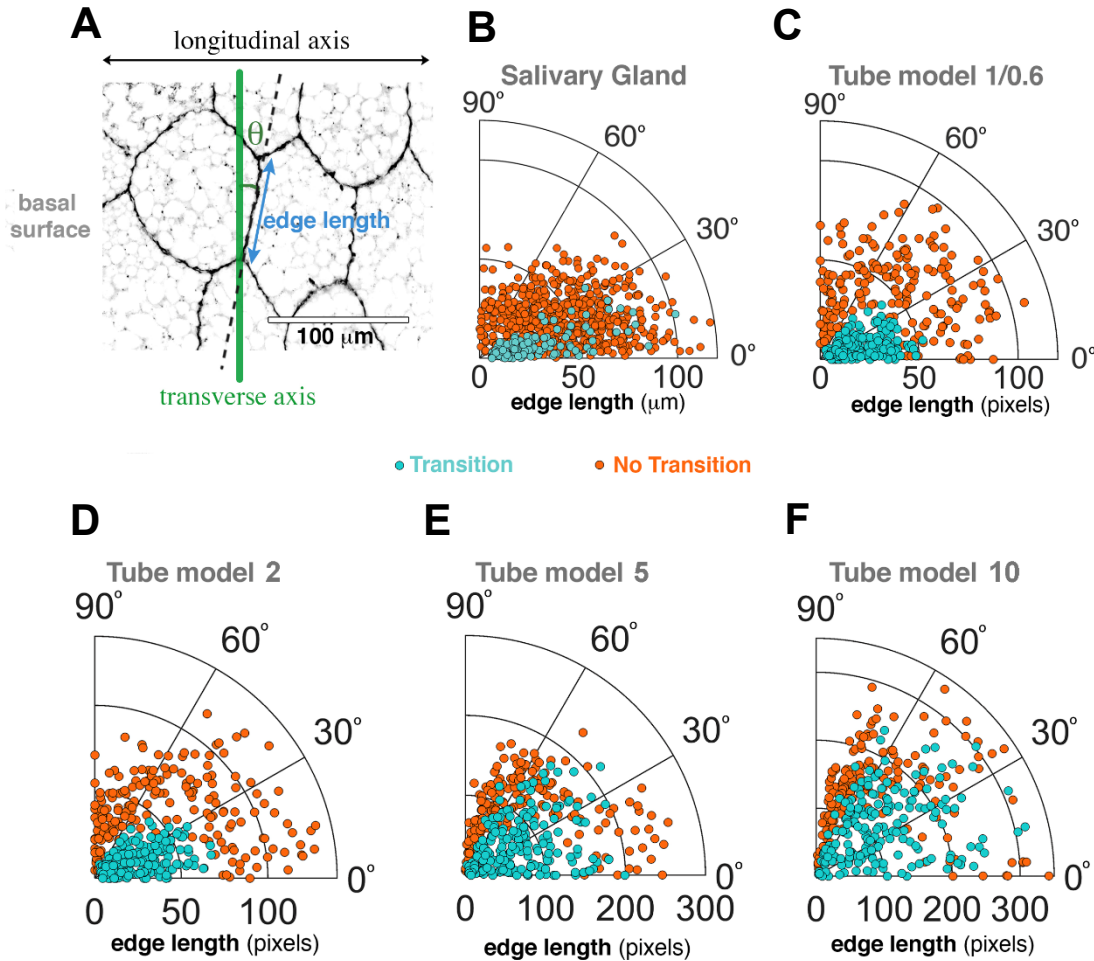


Figure 14. Geometric measurements from intercellular edges

A) Scheme showing the measurements guideline to extract edge angle and length measurements from the basal surface. The angle (θ) is always measured taking the transverse axis as 0° . Scale bar = $100 \mu\text{m}$. **B)** Polar scatter showing the cited measurements in the basal surface of salivary glands. **C)** Same than **B** but measured in the Voronoi tubular model, specifically on the layer with the same percentage of scutoids than the salivary gland ($SR = \frac{10}{6}$). **D-F)** distribution of edges angle and length for tubes at different SR : 2 (**D**), 5 (**E**) and 10 (**F**). The Voronoi tubes are formed with 200 cells ($n = 20$). The light blue dots embody the intercellular edges of 4-cells motifs that promote apico-basal transitions; The orange ones represent just the opposite, the edges without transitions.

regarding the transversal axis of the cylinder, ii) its lengths and iii) the presence of apico-basal intercalations (**Figure 14A**, 146 motifs with apico-basal transition and 656 without it). We found that the edges involved in apico-basal transitions were characterized by presenting lower angles (0 – 30 degrees) and shorter lengths, while the non-involved ones could be found in a wider range of angles and lengths (**Figure 14B**). Analogous results were obtained, in the Voronoi tube at the SR with a similar proportion of scutoids than the gland ($SR = 10/6$, **Figure 14C**)

Thereupon, examining these properties in all the screened SR of this Voronoi tube we got to the conclusion, in which, at smaller SR the shorter edges with an orientation closer to 0° resulted on transitions. Notwithstanding, the larger edges in a wider range of degrees of orientation could be involved in apico-basal cell intercalations as the SR grows (**Figure 14D-F**). These results were complemented by analysing the 4-cells motifs from apical to basal, that is to say, if we measured in apical, the shorter edges with angles close to 90° would favour the apico-basal transitions (**Figure 15**).

Remarkably, all the basal edges implicated in apico-basal intercalations presented a reduction of length until reaching the four-cells vertex and then expand again its size approximately at 90° of the original (basal or apical) orientation (**Figure 9C**, **Figure 10D** and **Figure 11B**). In conclusion, we found that the length and angle between transition and non-transition edges had different distributions (**Table 1**, **methods**). These data suggested that the cylindrical surfaces imposed a geometrical constriction to the cells based on the curvature anisotropy of this geometrical figure. In tubes, the SR is a simplification of the curvature anisotropy (or surface ratio anisotropy). Along this document this anisotropy will be formally measured by the formula: $(\frac{R_b^h}{R_a^h} / \frac{R_b^w}{R_a^w}) - 1$. Where h , stands for the axis of greatest curvature (transversal axis in Voronoi tube), w , for the axis of least curvature (longitudinal axis in Voronoi tube). R_a refers to the apical radius, while R_b is the basal one. For instance, R_a^w is the average Cauchy radius along the apical surface by considering the longitudinal axis (w). In tubes, this expression $(\frac{R_b^h}{R_a^h} / \frac{R_b^w}{R_a^w})$ could be replaced by the SR . Given that, $R_b^w = R_a^w = \infty$, being $\frac{R_b^w}{R_a^w} = 1$, and $R_b^h = SR \cdot R_a^h$, then $(\frac{R_b^h}{R_a^h} / \frac{R_b^w}{R_a^w}) = \frac{SR}{1}$. So, in tubes, the surface ratio anisotropy is $SR - 1$. In summary, the results of this section suggest that the difference of curvatures is a main factor inducing the presence of scutoids.

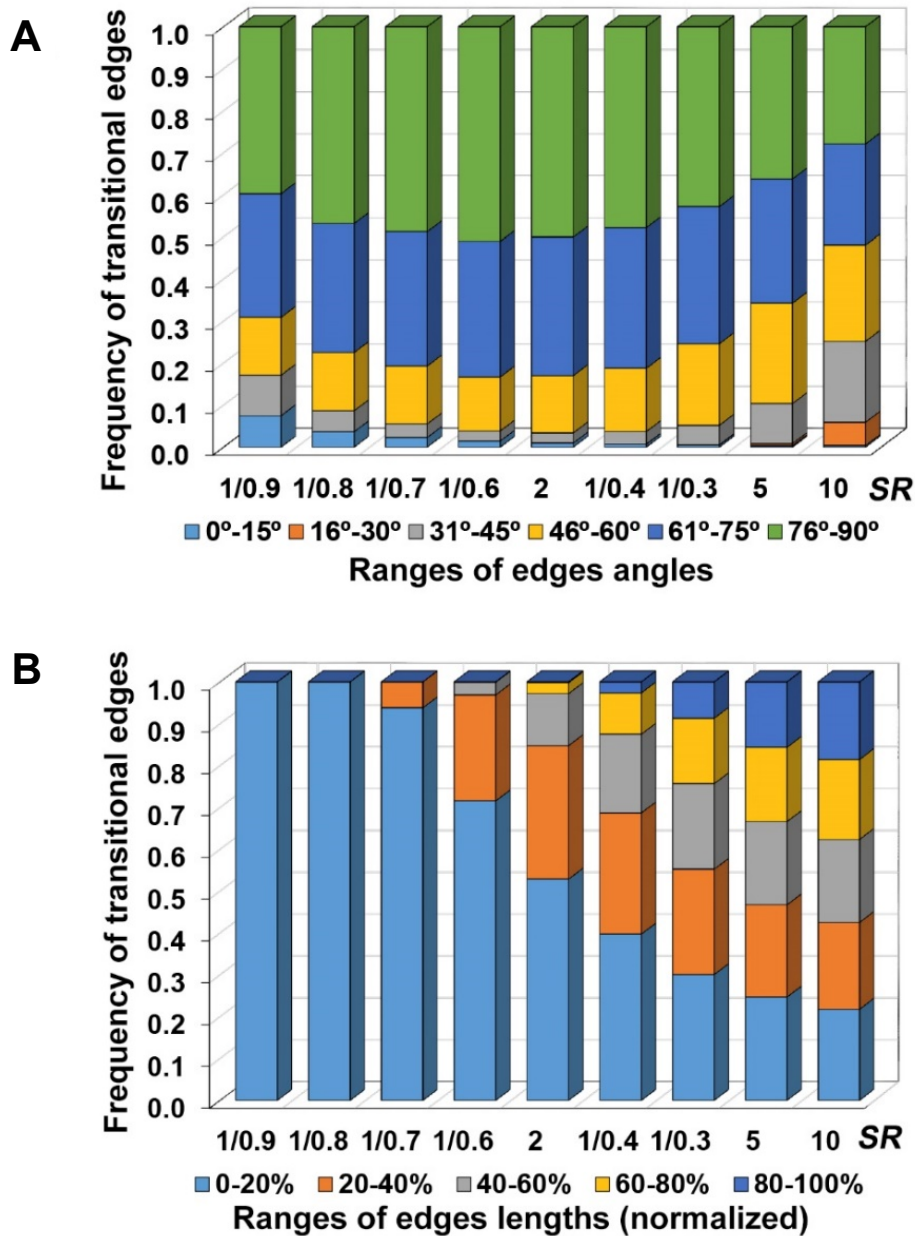


Figure 15. Measurements of transitional edge lengths and angles from apical

A) Diagram of frequency grouping the edges classified by angles (every 15 degrees) promoting apico-basal transition measured in tubes with 200 seeds ($n = 20$) at different surface ratio expansions. **B)** Similar diagram to **A** but grouping the edges length instead of the angles. These groups contemplate steps of 20% in relation to the maximum edge length (100%). As we can see in these diagrams, at smaller SR , the edges involved in cellular intercalations are mostly short (0 – 20%) and its angles close to 90° ($61^\circ - 90^\circ$), but with the increase of SR the range of edges lengths and angles get wider, homogenizing the frequency of all groups at higher surfaces ratios.

4.3. A general fact: the curved epithelia hold scutoidal cells

To investigate if the appearance of scutoids was a general feature of curved epithelia we have analysed other biological tissues. First, we studied the *Drosophila* embryo (**Figure 16A**) through confocal images supplied by our collaborator Dr Sol Sotillos (CABD, CSIC/JA/UPO, Campus Universidad Pablo Olavide, Seville), in which we examined two differentiated regions, one where the epithelial tissue folds forming invaginations and evaginations and another where the tissue is flatter (**Figure 16B**). Then, by tracking the cells along all the slices of the stacks of images (4 different embryos), we achieved to detect the presence of apico-basal intercalations (**Figure 16C**). We identified $50 \pm 15\%$ of scutoids in the folding regions (214 cells checked), and a $15 \pm 4\%$ in the flatten zone (734 cells checked), also with the geometrical measurements of angle and length over the cell outlines (**methods**). This quantification supports the previous underlying assumption from the analysis of the salivary glands, where the asymmetric curvature was characterized as a main factor responsible for scutoids emergence. In embryo folds, the surface ratio was higher ($SR = 1.6 \pm 0.2$) than in the control epithelium ($SR = 1.2 \pm 0.1$). We found a direct correlation between the proportion of scutoids and the observed surface ratio. In addition, we observed in the embryo furrows that the edges of motifs involved in apico-basal transitions were oriented in an angle smaller than 45° (regarding the transversal axis of the fold) (**Figure 16D**, right). These results resemble to the correlation found in the salivary glands.

Nonetheless, since in the embryo planar surface, the curvature anisotropy is soft ($SR = 1.2 \pm 0.1$), the edges involved in apico-basal intercalations presented lengths and angles less constrained than in folds (**Figure 16D**, left). Therefore, there was not a clear difference between the distribution of the lengths and angles of the edges implicated in transitions and in those that did not (**Table 1**).

The cases of study showed above have only considered tubular/folding structures where there is a null curvature that matches with the longitudinal axis. This feature represents an extreme case of curvature anisotropy. Therefore, we investigated other geometrical shapes with different curvatures such as a sphere, a dome or a spheroid. In this way, our collaborators Dr María D. Martín-Bermudo (CABD, CSIC/JA/UPO, Campus Universidad Pablo Olavide, Seville) and Dr Andrea Valencia Expósito (CABD, CSIC/JA/UPO, Campus Universidad Pablo Olavide, Seville) provided us with a set of confocal images from *Drosophila* egg chambers at different age stages. These biological structures are conformed by a set of joined germinal cells (15 nurse cells and 1 oocyte)

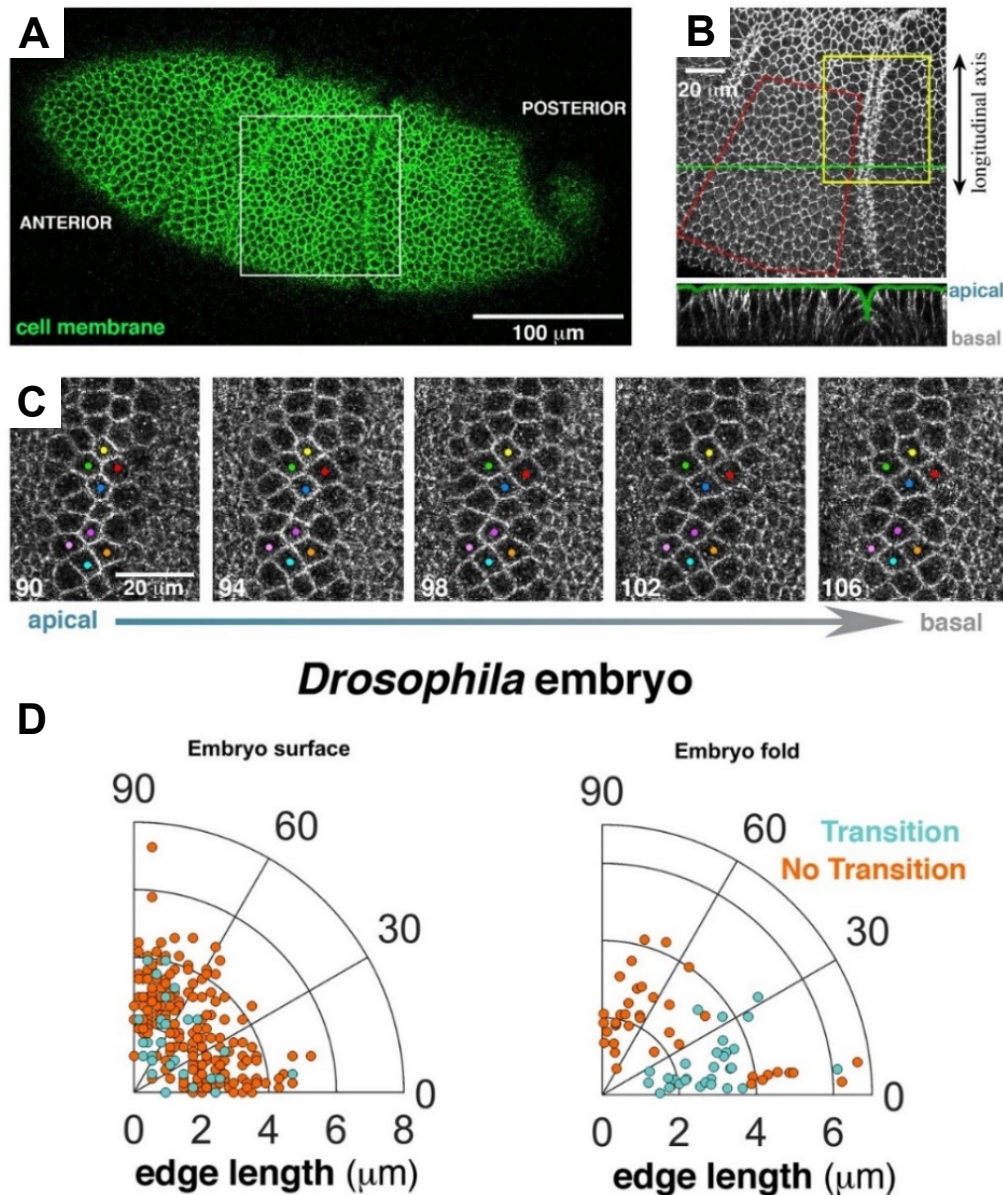


Figure 16. Scutoids found in *Drosophila* embryo

A) General view of *Drosophila* embryo at stage 6-7. The cell outlines are stained in green, also it is indicated the anterior and posterior regions. Scale bar = 100 μm . **B)** Zoom of the region of interest (ROI) in the posterior part, where the gastrulation folds are marked in yellow and the “areas without folds” in red. The double arrow designates what we have taken as a longitudinal axis to take the geometrical measurements over the tissue. A transversal view (sagittal) of the ROI is appreciated. Scale bar = 20 μm . **C)** Set of confocal sections along the Z-axis inside the yellow ROI (**B**) showing two four-cells motifs with apico-basal transitions (the cells are labelled with coloured dots). The numbers tag the confocal planes, starting in the apical surface (outer). Every confocal plane is separated by 0.3 μm . Scale bar = 20 μm . **D)** Polar scatters of the intercellular edges in four-cells motifs considering the flattened surface (left) and the folds (right) for transitional (light blue dots) and non-transitional (orange dots) edges.

surrounded by a monolayer epithelium, the follicle cells (**Figure 17A-B**). The development of the egg chamber is a well-studied phenomenon classified in a total of 14 stages, from an initial spheroidal egg (at stage 1) getting a shape similar to a prolate spheroid over the developmental course. Then, we focused on the follicle cells organization for several isolated stages: i) the stage 4 (**Figure 17A**) where the egg chamber embodiment shows an aspect akin a prolate spheroid where the longitudinal axis is not quite different to the

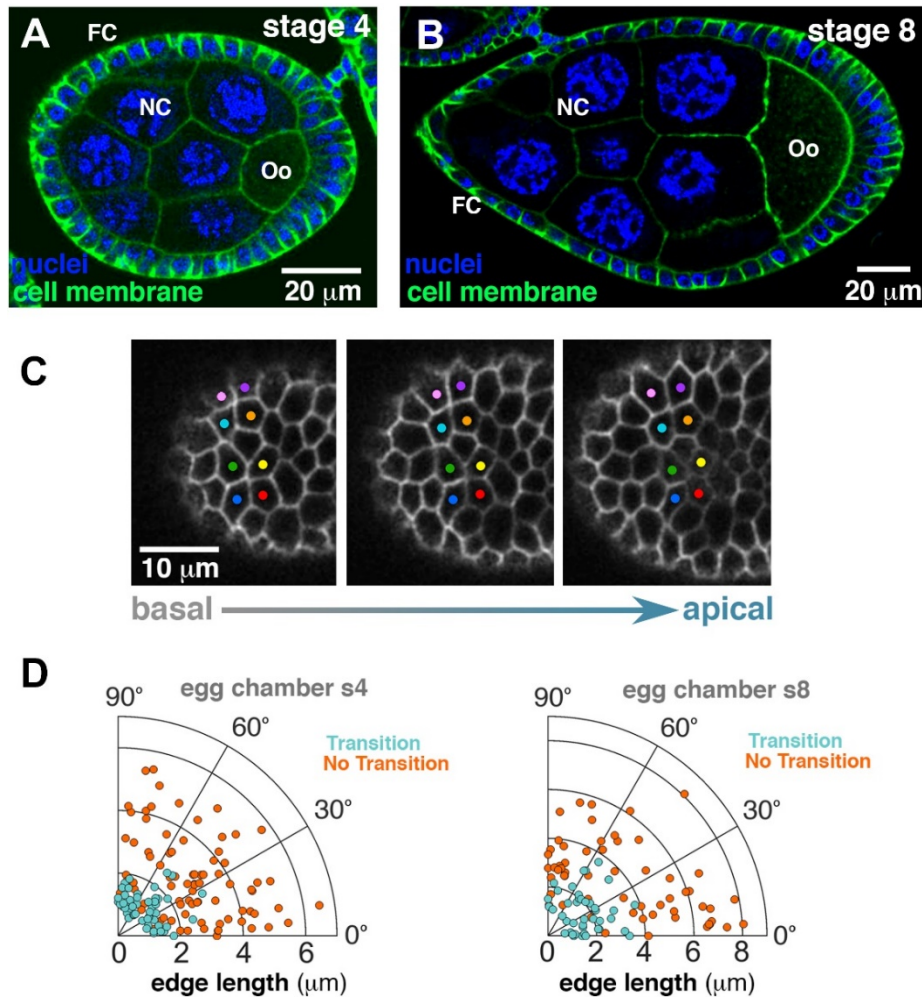


Figure 17. Scutoids presence in *Drosophila* egg chamber

A-B) Confocal section of *Drosophila* egg chamber at stage 4 (**A**) and 8 (**B**) of development. The nuclei are tagged in blue and the cell edges in green. It can be distinguished different type of cells: follicular cells (*FC*), nurse cells (*NC*) and the oocyte (*Oo*). Scale bars = 20 μm . **C)** Tracking of 2 transitional four-cells motifs (the cells are labelled with coloured dots) along the Z-stack at different Z-depth, from basal to apical taken with steps of 0.4 μm , over an egg chamber at stage 4 (**A**). Scale bar = 10 μm . **D)** Graphics with polar scatter showing the distribution of edge lengths regarding its angle in transitional (light blue) and non-transitional (orange) intercellular edges, at stage 4 (left) and 8 (right).

two others (mild elongation). ii) the stage 8 (**Figure 17B**) where after a rotation procedure and the coordinated migration of the follicle cells, the egg chamber elongates until to acquire a prolate spheroidal shape with a much longer longitudinal axis (complete elongation) (Jia et al., 2016). Presumably, in both states, it was found apico-basal transitions on the follicle cells (**Figure 17C, methods**), but the logic of the appearances differs with the proof of principle of tubular structures: the stage 4 when the anisotropy of curvatures is minor (i.e. a sphere belongs identical curvatures of all its axes. Then, it should not contain any scutoidal cells influenced by the geometry) owns a higher quantity of scutoids (13 samples, $20 \pm 8\%$ scutoids on 719 cells) than the stage 8 (14 samples, $10 \pm 3\%$ scutoids on 1283 cells) where the difference of curvatures is noticeable (**Table 2**). In the same way, the intercellular edges in basal whose four-cells motifs have been involved into neighbours exchanging along the apico-basal axis did not follow a predictable pattern, appearing with diverse orientations and lengths (**Figure 17D, discussion**).

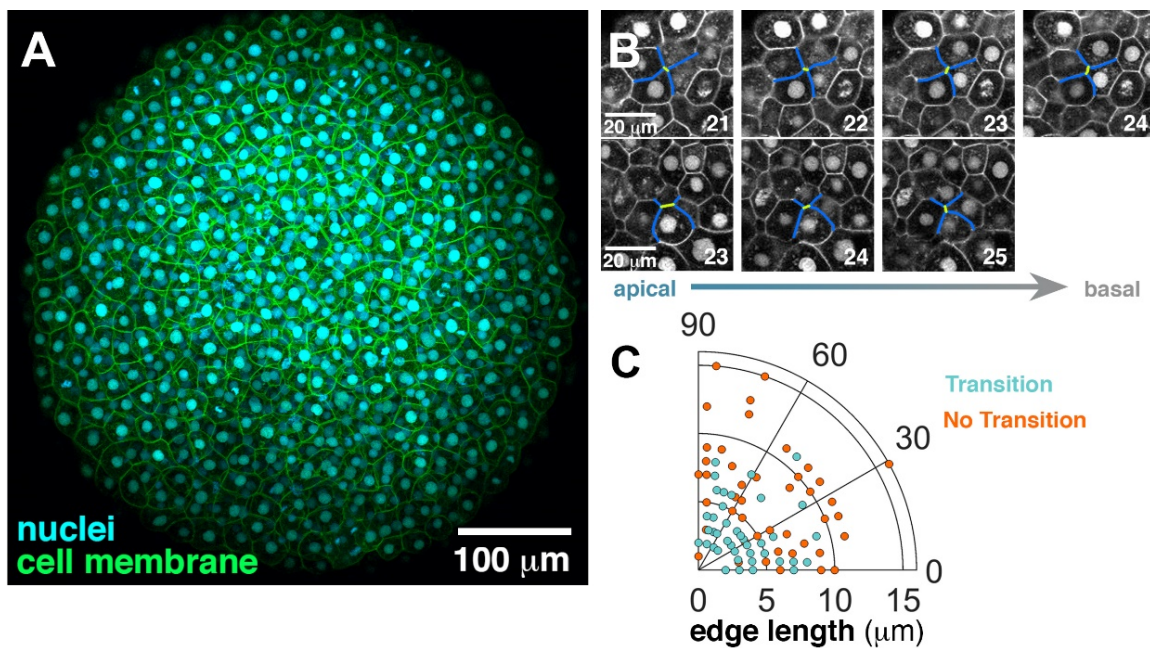


Figure 18. Scutoids are found in zebrafish epiboly

A) Confocal image of zebrafish embryo at 50% of epiboly, where the cell outlines are labelled in green colour and the cell nuclei in cyan. The exterior surface corresponds with the apical layer, while the inner is the basal one. Scale bar = 100 μm . **B)** Highlighted and zoomed regions at different Z-planes, tagged with numbers from apical to basal (Z step = 1.2 μm). It can be observed how the apico-basal transitions are carrying on over this tissue by following the coloured cells outlines (cell outlines in blue and intercellular edge in yellow) of the motifs. Scale bar = 20 μm . **C)** Polar scatter showing the distribution of edge lengths regarding its angle in transitional (light blue) and non-transitional (orange) intercellular edges, extracted from the outer epithelial layer of zebrafish epiboly at 50%.

Finally, we tried to corroborate if the presence of scutoids was a generalized fact on epithelial cells, and for this purpose, we studied a widely-used vertebrate animal model, the zebrafish. In this case, our collaborator Dr Florencia Cavodeassi (Centro de Biología Molecular Severo Ochoa, Madrid and St. George's University of London, London) provided us images at 50% of epiboly (gastrulation movement). At this stage of the epiboly could be visualized a set of germinal cells established in multilayers around a quasi-spherical embryo (**Figure 18A**). Surprisingly, we witnessed a $2.9 \pm 1.5\%$ of scutoids after examining 6724 cells on 7 different embryos (**Figure 18B**), demonstrating how this event is not exclusive of *Drosophila*. Despite finding scutoids in this species, we did not observe a tendency to predict the apico-basal intercalations emergence in terms of intercellular edge length and angle (**Figure 18C**), similarly than occurred on the *Drosophila* egg chambers (**discussion**).

4.4. Voronoi spheroidal models reproducing egg chamber structures

Motivated by the huge similarities found by comparing the Voronoi tubes with *Drosophila* salivary glands and embryo folds, we computed other Voronoi structures in which exists three non-null curvatures (in a tube the longitudinal axis owns null curvature). In particular, we have generated 3 variants of spheroid models with different axes length to test the presence of scutoids by elongating its shape: *sphere* (**Figure 19A**), *globe* (**Figure 19B**) and *zeppelin* (**Figure 19C**).

As expected, after checking the Voronoi cells on the *sphere* model, we did not find any scutoidal cell. Here, as in the rest of spheroid models, we computed three different apico-basal cell lengths, and the reason because this model didn't contain any scutoid is due to the proportional change of curvature between the apices and bases in all the three axes. Therefore, the isotropic change of curvature avoids scutoids formation. However, when the anisotropy slightly appears, for instance in the *globe*, the quantity of scutoids is directly proportional with the increment of cell height ($21.7 \pm 6.7\%$ at height 0.5, $43.5 \pm 7.7\%$ at height 1 and $61.6 \pm 10.1\%$ at height 2), and of course, these data are bigger when the asymmetry of curvatures raises, i.e. the *zeppelin*-like shape ($40.2 \pm 9.3\%$ at height 0.5, $68.7 \pm 9.2\%$ at height 1 and $89.2 \pm 5.1\%$ at height 2). Therefore, the mentioned anisotropy increases when the cell height became larger, being this circumstance the main factor for the scutoids emergence (the higher the anisotropy, the more the scutoidal cells will appear) (**Table 2** and **3**).

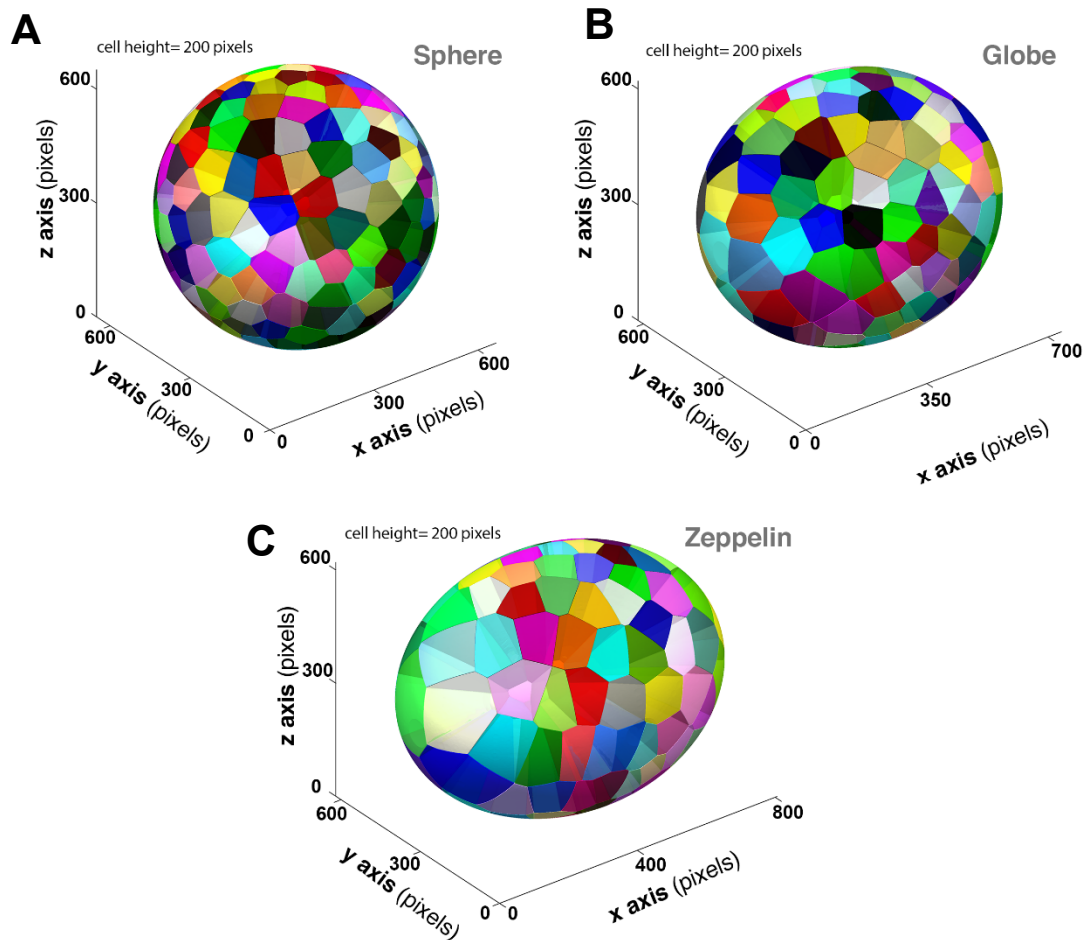


Figure 19. Voronoi spheroidal models

A-C) Voronoi spheroidal models with different elongations. The represented spheroids have the same Y and Z apical radius and the cell height is twice as much this value. The panel **(A)** represents a '*Sphere*' with its 3 axial-radii equals; **(B)** is a Voronoi spheroidal model with '*Globe*' shape: the X apical radius is 1.5 times the length of Y and Z apical radii; **(C)** shows a Voronoi spheroidal model with '*Zeppelin*' shape: the X apical radius is 2 times the length of Y and Z apical radii. **Methods.**

Once we carried out the sampling experiment from a sphere to a more oblate spheroid, we investigated the specific cases of egg chambers at stages 4 and 8 (**Figure 20A-B**). To do that, we developed spheroids resembling the egg chambers in some main characteristics: the three axes of curvature, the cells height and the cellular density (**methods**). A total of 130 simulations of "*stage 4-like*" spheroids and 30 of "*stage 8-like*" were developed, where 15285 and 7051 cells were analysed respectively, getting $6 \pm 4\%$ of scutoids for the first type of spheroid and $11 \pm 4\%$ for the latter (**Table 3**). Despite the *in silico* models imitated the geometry of the biological samples, the results of their analyses showed some clear dissimilarities when they are compared:

1. The number of scutoids obtained on these simulations (spheroids) matches with the previous computational experiments (tubes). The more the anisotropy the more the scutoids, i.e. spheroid *s8* had larger proportion of scutoid than *s4*. Nevertheless, in the natural samples occurred just the opposite, getting more scutoids in the egg chamber at stage 4 than at stage 8 (**discussion**).
2. The appearance of apico-basal intercalations on all the computational models is associated with the intercellular edge length and orientation (**Figure 20C-D** and **Figure 14C-F**). Nonetheless, the actual egg chambers did not show a preferential orientation of its edges when an apico-basal cell intercalation results on scutoidal cells (**Figure 17D**, **discussion**).

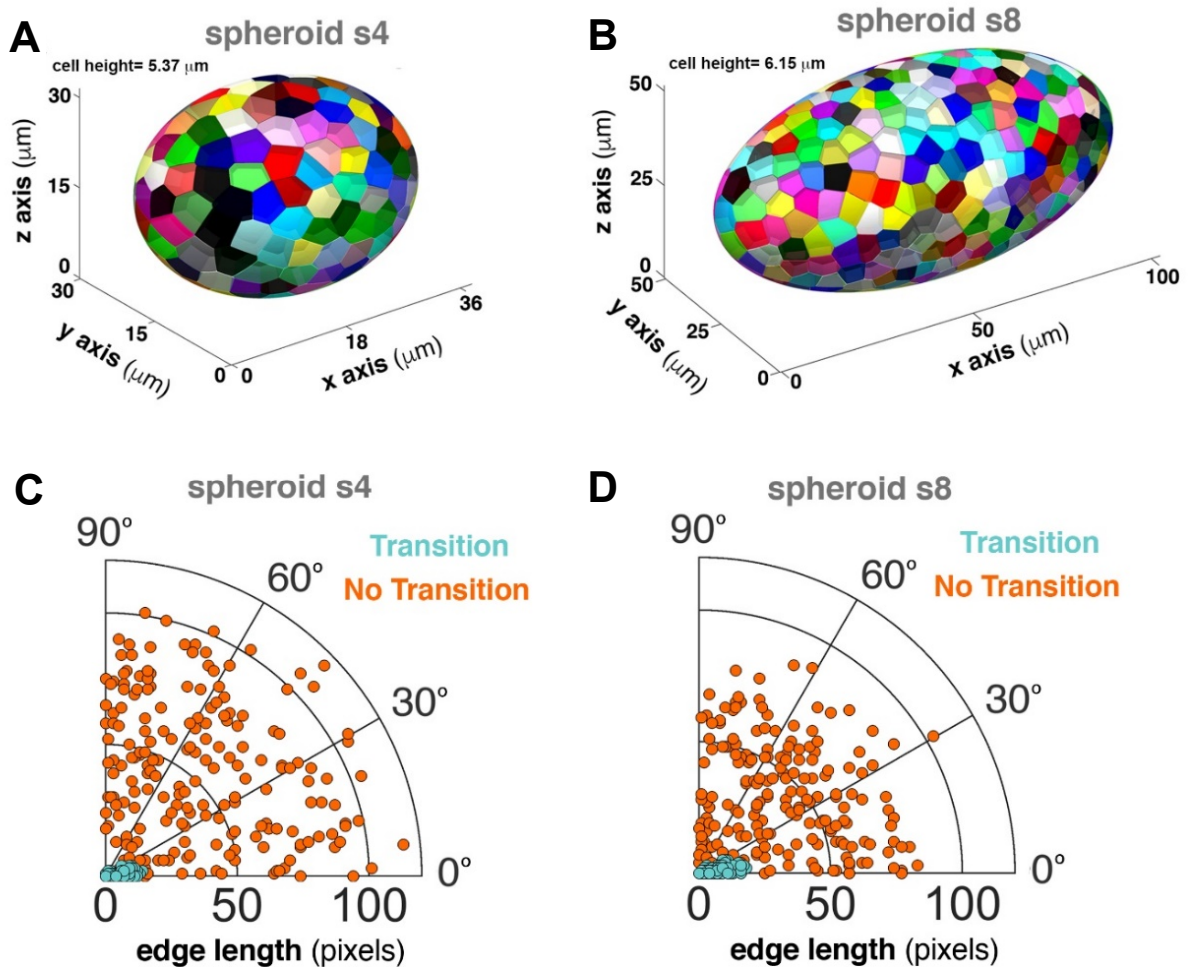


Figure 20. Voronoi spheroidal models imitating the egg chambers at stage 4 and 8 of development

A-B) Voronoi spheroidal models with the same dimensions and cell density (on average) than the egg chambers at stage 4 (**A**) and 8 (**B**) examined (**methods**). **C-D)** Polar scatters showing the distribution of edge lengths regarding its angle in transitional (light blue) and non-transitional (orange) intercellular edges, at models mimicking the stage 4 (**C**) and 8 (**D**) of egg chambers.

4.5. A biophysical model to analyse the apico-basal intercalations

With the support and expertise of the physicist Dr Javier Buceta, we used our Voronoi models and the data extracted from the epithelial tissues to explore the biophysical cues driving the appearance of apico-basal intercalations. This study aimed on adding information about the cellular 3D packing and the physical reason behind the scutoids emergence in diverse curved epithelia. In particular, we analysed the “line tension” component of the forces of the cells focusing on the changes between cells that participate or not on the spatial $T1$ transitions.

Based on a minimal model that explains how the line-tensions fluctuations could let $T1$ transitions (Spencer et al., 2017), Dr Javier Buceta proposed to use the same theoretical framework to study the spatial $T1$ transitions along apico-basal space. Here, our collaborator considered an initial state (apical), where a motif of 4-cells is represented with vertices and edges connections (**Figure 21A**), and a final state (basal) where could occur (or not) an exchange of neighbours. Specifically, each of these states could manifest combinations of two stable packing configurations of 4-cells motifs, S_w and S_h , where the length of its intercellular edge is defined by l_w and l_h respectively (**Figure 21B**). Anyway, intermediate states are characterized by a linear combination regarding the angle of the intercellular edge, that is decomposed in l_w and l_h .

$$l = \sin(\theta) l_w + \cos(\theta) l_h$$

Notwithstanding the foregoing, it could exist an unstable conformation in which the intercellular edge turned into a point where the four cells are connected ($l = 0$, $l_w = l_h = 0$). In this way, it was defined an energetic function focused on the tensors that manage the interactions of the cells (Bi et al., 2015; Hannezo et al., 2014; Lecuit et al., 2011). This energy could be calculated as a function of the intercellular edge angle (θ), the sum of all the edges length into the motif packing configuration (L_T), also including the aspect ratio ($\epsilon = \frac{\langle h \rangle}{\langle w \rangle}$, reporter of surface ratio anisotropy) of the 4-cellular motif (**Figure 21A-B**):

$$\hat{E}_{exp}^2 = (\hat{E}_{aux} \sin(\theta))^2 + (\hat{E}_{aux} \cos(\theta))^2, \quad \hat{E}_{aux} = \frac{L_T}{2\sqrt{(1 + \epsilon^2)}}$$

$$\hat{E}_{exp} = \sqrt{\hat{E}_w^2 + \hat{E}_h^2}$$

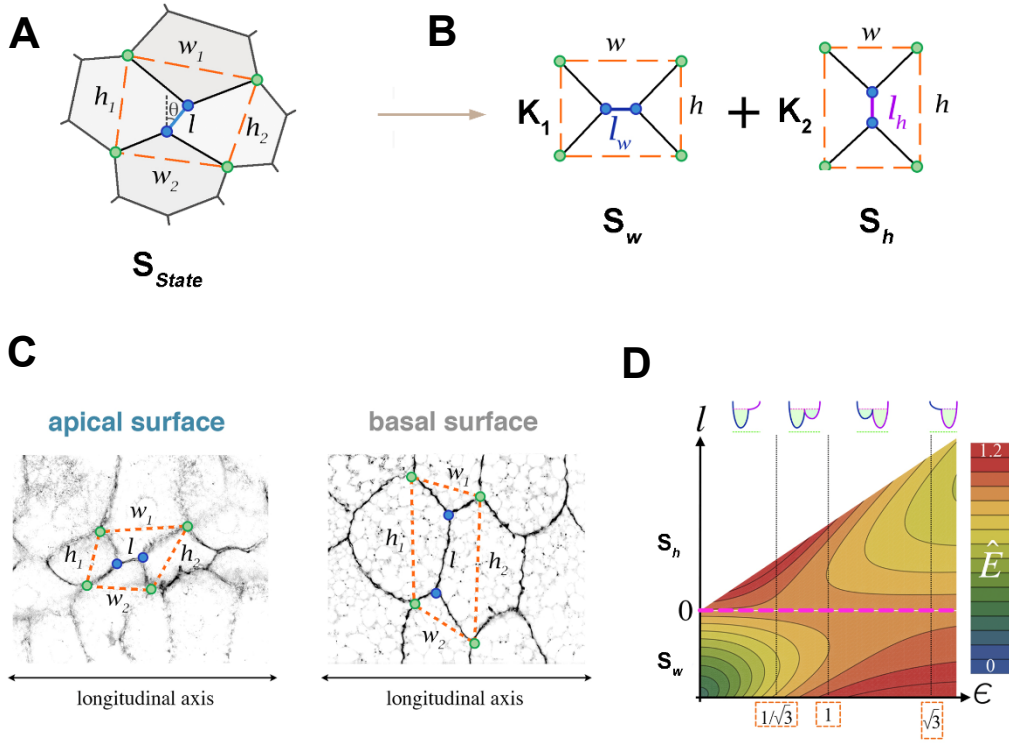


Figure 21. Line-tension minimization model applied to epithelia

A) Four-cells motif (S_{State}) with the measurements needed to feed the line tension model: $\langle w \rangle = \frac{w_1 + w_2}{2}$ (parallel to the longitudinal axis), $\langle h \rangle = \frac{h_1 + h_2}{2}$ (parallel to the transverse axis), l the intercellular edge length and its angle (θ) respect to the transverse axis. **B)** Decomposition in two idealized stable states S_w and S_h from the real four-cells motif (**A**, S_{state}), with the edge length characterized by l_w and l_h . The weight of each decomposed state would depend on the edge angle: $K_1 = \sin(\theta)$ and $K_2 = \cos(\theta)$. **C)** Illustration of the mode in which we carried out the measurements over the actual confocal images in salivary glands, where $\epsilon = \frac{\langle h \rangle}{\langle w \rangle}$ and l are clearly different from apical to basal. **D)** Density plot relating the theoretical energy model, ϵ and the predominant state of the four-cells motifs (S_h or S_w). When $\epsilon < \frac{1}{\sqrt{3}}$ the only stable state is S_w , if $\epsilon > \sqrt{3}$ the only stable state is S_h , and both states (S_w and S_h) are stable between these values ($\frac{1}{\sqrt{3}} \geq \epsilon \geq \sqrt{3}$). When a transition between $S_w \leftrightarrow S_h$ from apical to basal takes place, the scutoid cells appear. The dashed magenta line indicates an unstable configuration when $l = 0$ (cross). At the top, the wells indicate the energy profile within each ϵ zone: the green-shaded regions indicate the stable energy attractors and the green dotted line the absolute energy minimum.

The apico-basal transitions can be defined as a change of state $S_w \leftrightarrow S_h$ (**Figure 21B-C**) bypassing the unstable state of the energetic landscape (**Figure 21D**) where $l = 0$, to another more energetically stable. This assumption has been represented in a density plot where the location that would occupy each cellular motif depends on ϵ , its current state (S_w or S_h) and the edge length, l (**Figure 21D**). So, in tubular tissues, sometimes is necessary that a 4-cells motif jumps an unstable energetic limit while changes its aspect

ratio along the different *SRs* (due to the tubular anisotropy). This jump is promoted by the appearance of apico-basal transitions, holding the cell motif in an energetic stable state. On this wise, we made the topological measurements needed to explore the energetic landscape of the cellular configurations. Then, Dr Javier Buceta analysed the energetic behaviour of transitional and non-transitional motifs in both salivary glands and *in-silico* model, in terms of \hat{E}_w and \hat{E}_h . More precisely, he assessed the energetic trajectories between the apical and basal conformations of the same cellular quartets (**Figure 22A-B**). When he studied these trajectories on cell motifs without intercalation, obtained disorganized and tiny changes between the apical and basal situations, that means small movements over the energetic attractors regarding the wide landscape (**Figure 21D**). On another note, it was ascertained long and sorted relaxing trajectories in the transition cases, due to a jump from an energetic attractor in apical to another in basal (or vice-versa), avoiding the unstable state (**Figure 22**, purple dotted line) and reaching a steadier

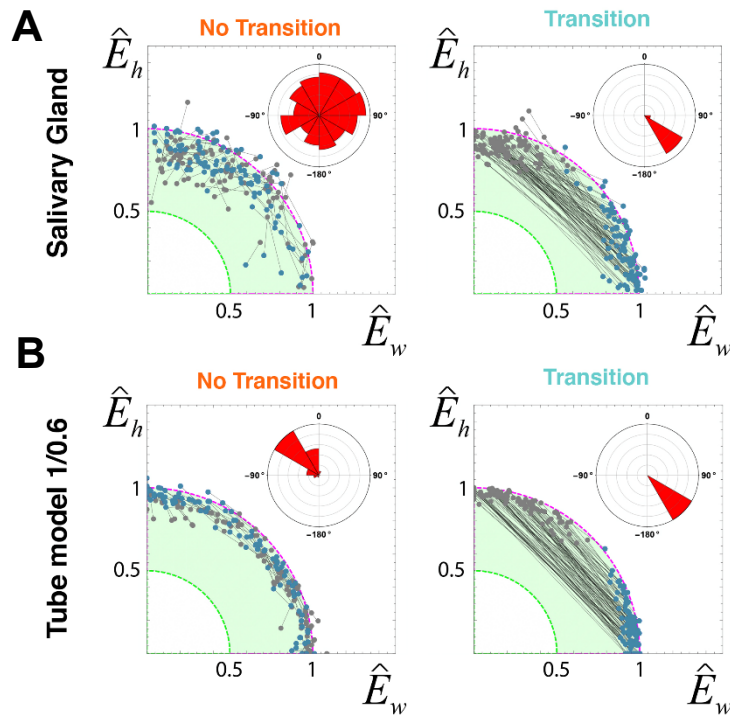


Figure 22. Tracking of energetic states

Decomposition of tensile energy into the fundamental energy states \hat{E}_w and \hat{E}_h , tracking the individualized four-cells motifs along with its basal (grey) and apical (blue) surfaces **A**) in salivary glands and **B**) in the Voronoi tubular model resembling the same percentage of scutoids than the glands. The non-transitional events are illustrated at left while the transitional is positioned at right. The dotted lines in magenta and green colours stand for unstable states where the quartet of cells would be joined by a vertex, and the minimum value of energy respectively. The stable attractors of energy are encapsulated into the green-shaded region. The polar histograms indicate the frequency and direction of trajectories from basal to apical.

condition (**Figure 22**, green area). Interestingly, we found a very similar behaviour between the biological and the computational samples, matching with the framework proposed by the theoretical line-tension model that anticipates the energy minimization as a working basis.

Lastly, when we examined the energetic cell configurations between the apical and the basal surfaces of the egg chamber-like spheroidal models, they matched with the Voronoi tubular model. These models presented unidirectional long relaxing trajectories on apico-basal transitions and shorter multidirectional trajectories into the region of stability for non-transitions (**Figure 23A**). In this way, all the Voronoi models couple the cells in every topological space maintaining the stabilization of all the local cellular motifs. Anyhow, the natural egg chambers exhibited relaxing trajectories with double directionality (**Figure 23B**) that suggested some biological processes that have come into play besides the topological circumstances (discussion). Consequently, as it has been demonstrated in models and in biological samples: the presence of scutoids supports the energetic stabilization of the epithelial 3D packing in curved topologies with anisotropic conditions, avoiding situations of instability that could appear if the scutoids performance would not take place.

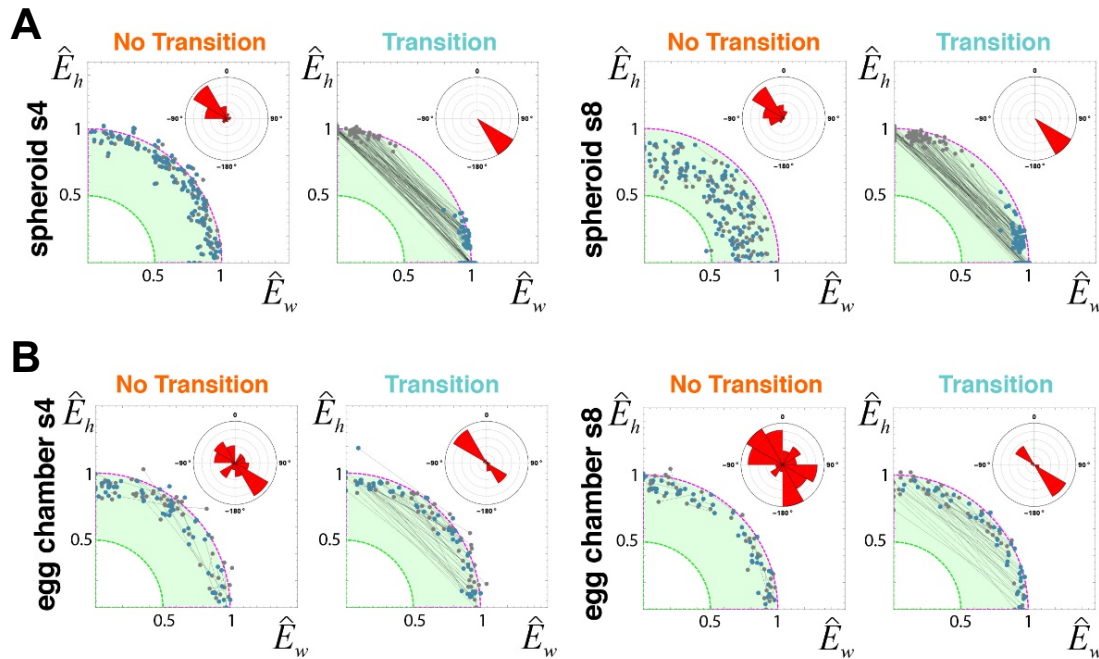


Figure 23. Energetic trajectories in egg chambers and its associated models

A-B) Linear decomposition of the experimental energies into the two idealized modes \hat{E}_w and \hat{E}_h calculated in both actual and *in silico* egg chambers at stage 4 and 8. The colour code is similar to **Figure 22**.

DISCUSSION

The embryogenesis, organogenesis and the full-body establishment at large, are managed by a precise morphogenetic plan that implicates complex cellular movements, folding or invaginations. The final formation of any curved epithelium requires a fine-tuning at the cellular level along the three dimensions. The cells that constitute the epithelia must cover two surfaces (the apical and the basal) that, in curved surfaces, differ in size between them (Nelson, 2016). Hitherto, the accomplishment of the cells as the building blocks of non-planar epithelia has been conceptualized by the enlargement or reduction of one surface regarding the another, conferring the frustum or truncated-pyramid shape to these cells (Lecuit and Lenne, 2007; Pearl et al., 2017) (**Figure 9B**). In this work, we have tried to analyse in-depth the 3D epithelial packing through the use of computational modelling based on the Voronoi mathematical rules. In this way, we put forward that using this kind of model, it is possible to simulate realistic curved epithelium architectures like tubes, spheres or spheroids. In spheres, the inner and the outer surfaces are proportional in terms of area in all the axes, while spheroids and tubes are not. That is to say, if we move from the inner surface to the outer one is needed an anisotropic change, where the inner surface should increase in one axis more than others until conforming the outer surface. According to our models, when the surface ratio anisotropy appears it is possible to find apico-basal cell intercalations (**Figure 10D, G**). In these cases, some cells adopt an undescribed geometrical shape to solve this packing problem (**Figure 10E**).

We have observed numerous cellular intercalations on anisotropic epithelial structures (i.e. salivary glands, embryos and egg chambers of *Drosophila* (**Figure 11A-B, Figure 17C, Figure 18B**)) reinforcing the prediction provided by our simulations. After confirming the presence of this solid in nature and in our simulations, we named “scutoid” to this geometrical entity. The particular shaping of the scutoid facilitates the exchange of neighbours along the apico-basal axis in curved and anisotropic topologies. The cited geometrical shapes are bounded between two parallel surfaces (apical and basal) and they own three main properties: i) their apices and bases are necessarily polygons (and all the other parallel surfaces between them) ii) can present a mix of concave and convex surfaces that make possible a set of scutoids fitting together seamlessly. iii) have at least a vertex along the apico-basal axis that enables having different neighbours between its two surfaces.

Our model has the capability of predicting apico-basal transitions when several topological conditions are satisfied. Particularly, the Voronoi tubular model explains how an increment of surface ratio ($\frac{R_b}{R_a}$) induces an augmentation in the number of scutoids. It

also agrees with the preferential orientation of the cells that promote the apico-basal transition: 4-cells motifs with its intercellular edge close to 0° regarding the transversal axis in the basal surface, will develop more easily an apico-basal transition resulting in a central edge close to 90° in apical, and its subsequent cell neighbouring exchange (**Figure 10D, G, Figure 11B**). These data in conjunction with the measurements of shorter edges that facilitate the apico-basal cells intercalations in the Voronoi models (**Figure 1C-F, Figure 15B**), match with the observed biological cases of larval salivary gland (**Figure 14B**), embryo folds (**Figure 16D**) and egg chamber of *Drosophila* in stage 8 (after stopping the cell proliferation and growing) (**Figure 17D**, right). However, not all the natural data can be explained by our models. For example, for any surface ratio anisotropy, the number of scutoids is larger in Voronoi models than in nature. This lesser proportion of scutoids in nature on stationary states might be a consequence of the cell's biophysics, its plasticity or surface stress, the biological procedures carried out internally, or external forces exerted by the surrounding environment. The Voronoi model only takes into account pure math factors, and does not considered other biological or physical effects.

Interestingly, we found other disagreements when contrasting the data from the egg chambers of *Drosophila* in stage 4 and the Voronoi spheroidal models simulating its dimensions and curved architecture: the percentage of scutoids is larger in the egg chamber than in the model, as well as we cannot find a relation between edges orientation and presence of apico-basal transitions (**Figure 17D**, left). The egg chamber from stage 1 until reaching the stage 8 is involved in a very dynamic procedure of enlargement in which the cells are migrating and the whole structure is rotating around itself (Cetera and Horne-Badovinac, 2015). To explain the discrepancy on stage 4 of the egg chamber, where the percentage of scutoids is larger in nature, we rely on a recently published study (Sun et al., 2017). This work explains how dynamic tissues could trigger the rearrangement or intercalations of the cells by means of basolateral protrusions, and this could be identified as dynamic scutoids immersed in biological reorganizations. This hypothesis gains strength when we examined a quasi-spherical epithelium, the zebrafish embryo at 50% of epiboly (**Figure 18A**). Here, our model predicted a tissue full of frusta (like a Voronoi sphere, **Figure 19A**) due to the embryo surface curvatures were very similar in all directions, nonetheless, some scutoidal cells were found. We argument the active cellular and morphogenetic processes as the main responsible, similar to what we observed in egg chamber at stage 4.

In this thesis, we explain that it is possible forming 3D curved structures by means of cells with a frustum or scutoidal shapes, but always tending towards the most efficient packing. Accordingly, our collaborator, the physicist Dr Javier Buceta, supported us to

explore the scutoid energetic implications over the tissue packing. The approach that we used, was inspired on the well-known $T1$ transitions (**Figure 9C**) that stabilizes the tissue along the time (Collinet et al., 2015; Osterfield et al., 2013). We have used a tensile energetic model that shows how a change in cellular aspect ratio manages the cellular rearrangement (Chen and Brodland, 2000) over time. This method was modified by replacing the time dimension by the spatial one, considering the “apico-basal axis” in particular. However, we are aware of other forces components acting during $T1$ transitions such as the cortex contractility, the cell turgidity, or the membrane stress, which likewise could be involved in the scutoids management. Nonetheless, we focused on the microenvironments of 4-cells motifs to study the line-tension on local curvatures in the cases with and without apico-basal transitions. The results of this analysis concluded that the presence of transitional motifs (i.e. scutoids) promoted the appearance of larger energetic trajectories that jumped unstable states and helped to stabilize the local cellular motifs (**Figure 22A-B**, **Figure 23A-B**, transition cases). The analysis of other possible forces components, for example contractility and elasticity, was strategically dodged to be interpreted in future works.

Parallel to our investigation, contemporary works from Dr Hinton, Dr Saunders and Dr Röper labs have also noted the presence of $T1$ spatial transitions in curved epithelia supporting our study (Rupprecht et al., 2017; Sanchez-Corrales et al., 2018; Xu et al., 2016). Besides, a recent work has shown how scutoids appear in soap bubble froth constrained between two tubular surfaces (Mughal et al., 2018). This article reinforces our theory: the scutoids make possible the minimization of the tissue energy and stabilize the three-dimensional packing.

Upon we have widely investigated how the tissues and models behaved in very different curvature situations, we tried to make a simplified and easily understandable model to explain the 3D epithelial packing. First, we modelled the simplest case of curved epithelia: a hollow cylinder surrounded by cells. In these cylinders, the curvature along the longitudinal axis is null, meanwhile, along the transverse axes, the two other curvatures are positive and equal, being its value dependent on the cylinder radius ($curvature = 1 / radius$). Regarding this model, a larger difference of curvatures between the basal and apical layers correlates with a higher proportion of scutoids. This difference of curvatures is given by the dimensionless surface ratio ($SR = \frac{\hat{R}_b}{\hat{R}_a}$), being \hat{R}_a the apical radius and \hat{R}_b the basal radius. When this parameter has the value $SR = 1$, all the cells should be prisms with identical apices and bases (**Figure 24**, dashed black diagonal arrow pointing to prism solid). However, if the surface ratio is slightly superior to 1,

all the cells could have a frustum behaviour (**Figure 24**, dashed blue arrow pointing to frustum solid), but depending on the initial configurations of the intercellular edges of 4-cells motifs, the tissue could present some scutoids at SR states close to 1 enabling a mix of frusta and scutoids (**Figure 24**, dashed blue arrow pointing to frustum+scutoid solids). Furthermore, it is possible reaching a 100% of scutoids for a heterogeneous distribution of edges length and orientations with bigger values of the surface ratio, for example, our Voronoi tubular model (starting from a Voronoi diagram 5 (**methods**)) reached it approximately at $SR = \frac{10}{3}$ (**Figure 13A and Figure 24**, dashed blue arrow pointing to scutoid solid). Along the document, we have explained the tissue behaviour just expanding from an apical surface to a basal one, but our model states that a reduction from the initial layer (basal) to an inner surface (apical) would get similar results. So, just considering the initial diagram as basal and the reduced surface as apical (**Figure 24**, the two triangles in which the figure is divided by the dashed black diagonal arrow).

After enunciating the simplest and the most clarifying model for understanding when the scutoids take place, we have extrapolated that to a more general plane where it is contemplated the coexistence of three non-null curvatures (spheres and spheroids) (**Figure 19, Figure 20A-B**). In this model, the surface ratio anisotropy is considered as the important factor influencing the appearance of scutoids. The surface ratio anisotropy can be explained as the relation between the SR along the major axis with the SR of the minor axis. When the SR of the minor and the major axes are identical, we are facing a spherical structure (**Figure 19A**), where scutoids should not exist due to the aspect ratio (ϵ) of the 4-cells motifs, being the same in both apical and basal surfaces. Notwithstanding, in spheroidal architectures where the SR of the major axis differ from the SR of the minor one, the aspect ratio of cell motifs in basal will probably mismatch from apical. So, for a fixed length of the minor axis and a fixed cell height in a spheroid, the longer the major axis (more prolate spheroid) the higher the proportion of scutoids. The more prolate the closer the structure to the most extreme case, the Voronoi tube, that is a result of one of its curvatures being null (along the longitudinal axis). Thus, the presence of scutoids is maximized (**Figure 25**).

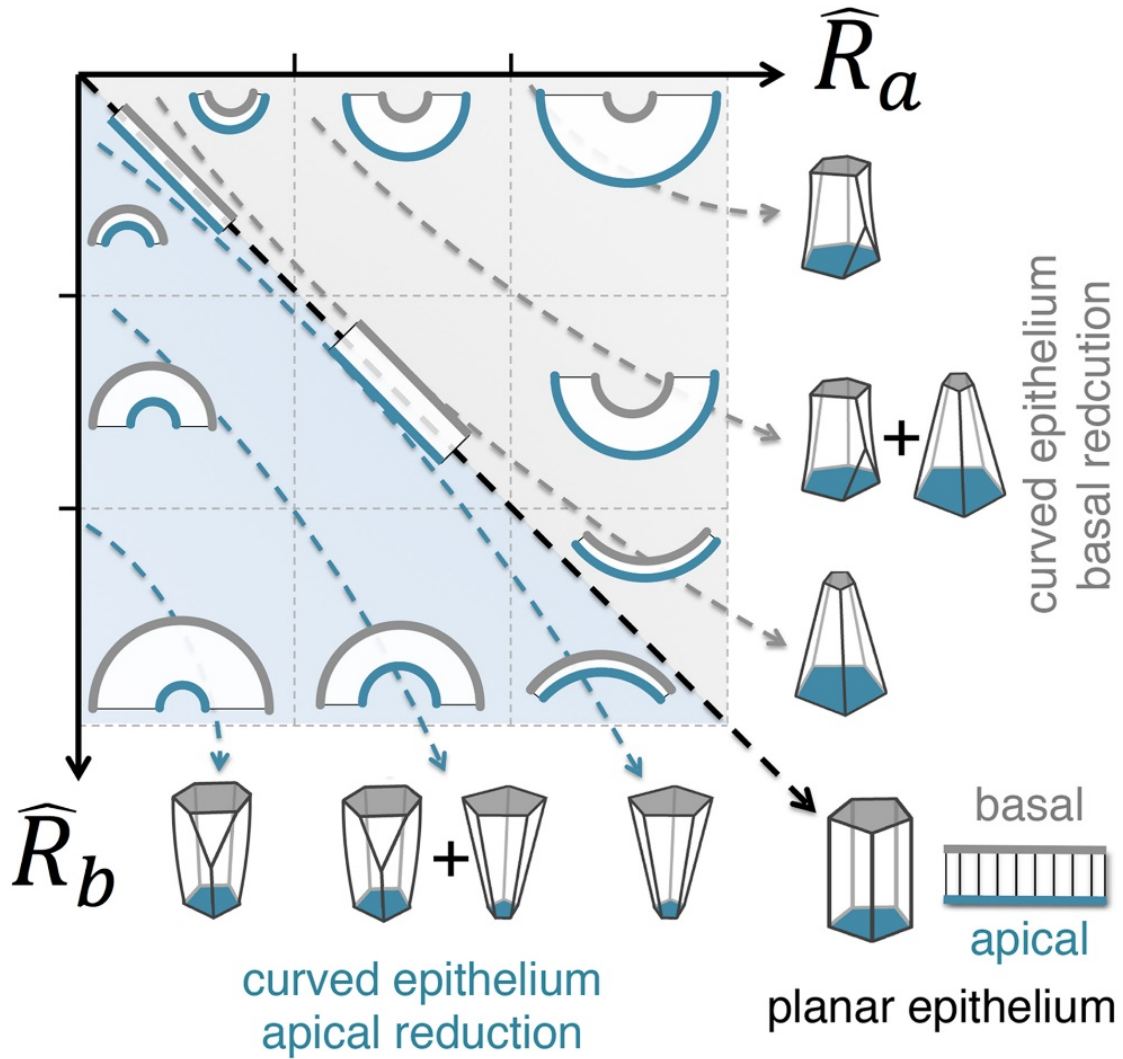


Figure 24. Summary of three-dimensional packing assuming at least a null curvature

This scheme shows how organizes the cells in three dimensions respect of the surface ratio ($SR = \frac{\widehat{R}_b}{\widehat{R}_a}$, when basal is outer than apical represented by the bottom light blue shaded triangle and, $SR = \frac{\widehat{R}_a}{\widehat{R}_b}$ when is inner, top light grey shaded triangle), that performs as the indicator of curvature anisotropy in tubular shapes. The black dashed diagonal arrow indicates the case of the planar epithelium ($SR = 1$) constituted by prisms. The curved dashed arrows point to the more favourable solids configurations depending on the tissue curvature: close to the black diagonal we could get preferentially frusta (bottom-right); if we get the situations with a bit more curvature anisotropy could get a mix of frusta and scutoids (middle-bottom and middle-right) and if go to the extreme tissue differences of curvatures the set of solids may be all scutoids (top-right or bottom-left).

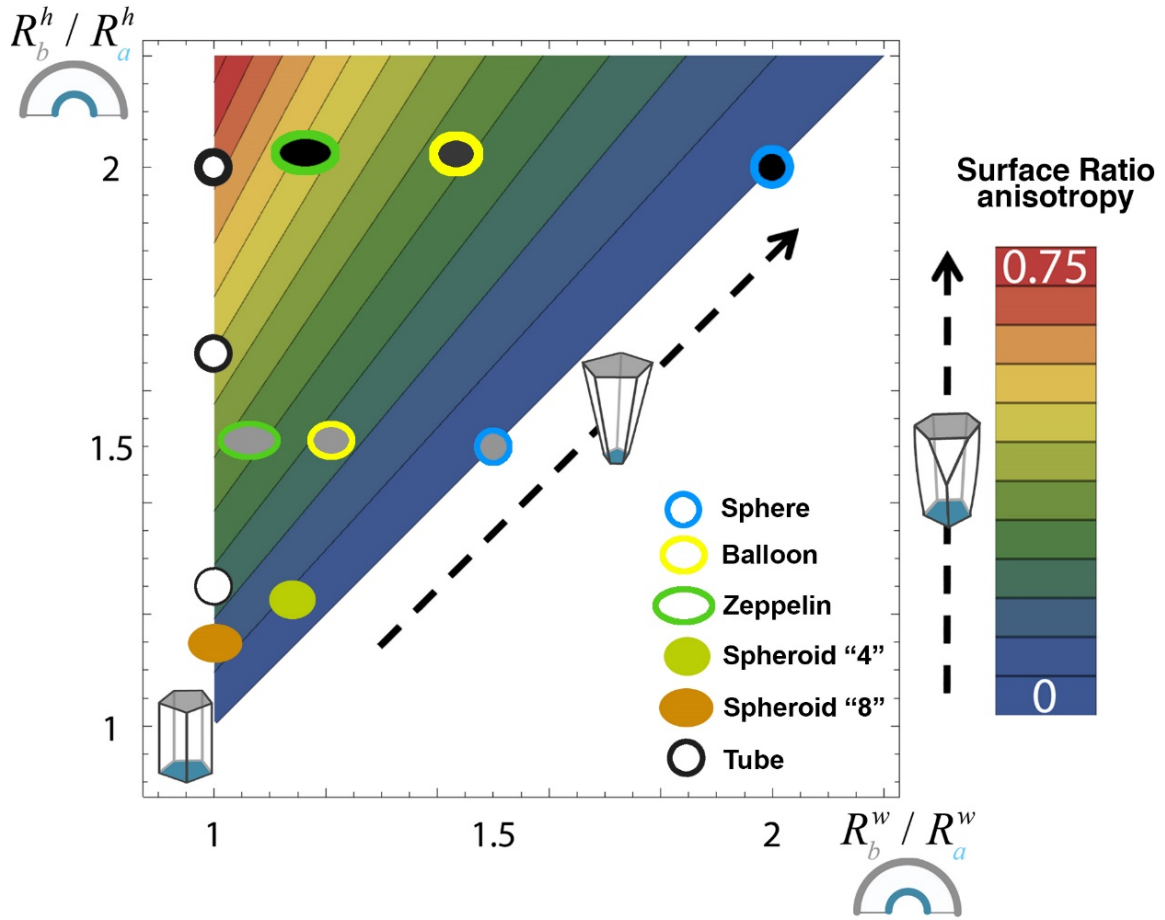


Figure 25. General 3D model considering 3 positive degrees of curvature

This model takes advantage of the two main axes of curvatures, that it is the minor (h , transversal) and the major (w , longitudinal) axes. R stands for the Cauchy radius, e.g. R_a^w is the Cauchy radius along the apical surface by considering the longitudinal axis (w). With this model is possible to achieve the calculation of the surface ratio anisotropy (colour palette at right) by testing the relative change of the aspect ratio between the apical and basal layers:

$\left(\frac{R_b^h}{R_a^h} / \frac{R_b^w}{R_a^w}\right) - 1$. As a result, the increase of surface ratio anisotropy is directly correlated with the augmentation of scutoids presence. Over this model we have represented some of our computational models: *sphere*, *zeppelin* and *globe* with 2 different cells heights, the spheroids 's4' and 's8' with an unique cell height, and the tube with 3 different cells heights. The wider the outlines the higher the cell heights. Here we have always taken the inner surface as apical and the outer as basal.

Our modelling approach together with detailed confocal imaging of epithelia let us know how cells realistically pack in curved surfaces. However, numerous are the questions that have turned up and remain unanswered. Probably, apico-basal intercalations during the development are very well-regulated and the factors involved in these tissue dynamics are currently unknown. So, we accept the challenge of deciphering them in the near future, by obtaining information from curved epithelial tissues in homeostatic and mutant conditions that affect the establishment of the epithelial architecture. It now becomes important to investigate how this new framework affects distinct processes during development and disease, from the morphogenesis of organs to the environment at the onset of tumour formation. For example, from a medical point of view, it has been recently shown how tissue curvature affects tumour progression due to the imbalance of tensions in apical and basal surfaces of epithelial tubes (Messall et al., 2019).

The possibility of generating human 3D cultures that resemble specific organs (organoids) has opened up enormous possibilities in biomedicine. However, recent advances in organoid technology, although highly promising, are hindered by its current lack of reproducibility. We strongly believe that the combination of engineering and developmental biology approaches will enhance the reproducibility and security aspects of organoid research (Clevers, 2016; Huch et al., 2017). We think that an accurate understanding about how the cells self-organize and modify its packing (included the scutoids fundamentals), might help to have complete control over organoid cultures. Altogether, the realistic analysis of epithelial packing would provide an advance in the biomedical field, especially in tissue and organ engineering (Hendow et al., 2016; Lecuit and Wieschaus, 2002; Yin et al., 2016). This advance could help to improve different aspects of biomedicine such as personalized medicine, drug testing, regenerative medicine, or disease modelling.

In summary, our contribution has unveiled unknown concepts regarding the cell packing properties, explaining how the cells pack in an efficient way being able to adopt an undescribed shape until now, the scutoid. This 3D organization system is the solution that nature has found to pack the cells when epithelia are anisotropically curved.

CONCLUSIONS

1. Our Voronoi tubular model simulates a tubular epithelium and predicts cells intercalations along the apico-basal axis. These intercalations induce an exchange of neighbouring cells between the apical and basal surfaces.
2. The presence of a novel 3D geometric entity allows these cells intercalations. We named this structure as “scutoid”.
3. A scutoid is a geometric solid bounded between two parallel surfaces (apical and basal). The scutoids own three main properties: i) their apices and bases are necessarily polygons (and all the other parallel surfaces between them) ii) can present a mix of concave and convex surfaces that make possible a set of scutoids fitting together seamlessly. iii) have at least a vertex along the apico-basal axis that enables having different neighbours between its two surfaces.
4. We have found scutoids in different model organisms after examining *Drosophila melanogaster* (salivary glands, embryo and egg chambers) and zebrafish embryonic epithelia.
5. The proportion of scutoidal cells in Voronoi tubular models is not dependent on cell density. However, it is strongly associated with the cell outlines orientation and length, and importantly, the higher the surface ratio, the larger the percentage of scutoids.
6. The Voronoi spheroidal model follows the same geometric constrictions than the Voronoi tubular model, where cell edges length and orientation are feasible indicators of the apico-basal intercalations presence. Furthermore, the larger the surface ratio anisotropy, the higher the proportion of scutoids.
7. In epithelia, scutoids could emerge as a result of cellular rearrangement along with morphogenetic movements (i.e. egg chamber of *Drosophila* and zebrafish embryo), enabling its presence in planar or spherical actual tissues. Thus, the scutoids appearing in nature, unlike Voronoi models, could not only be influenced by geometric constrictions.

8. The presence of scutoids supports the energetic stabilization of the tissue in terms of line-tension energy.
9. Based on the geometric constrictions imposed by the Voronoi tubular model, planar or tubular epithelia with $SR = 1$ should be formed only by cells with prismatic shape. When the SR is slightly bigger than 1, all the cells should have a frustum shape. Otherwise, the larger the SR the higher the proportion of scutoids. If the proportion of scutoids does not reach the 100% the remaining cells should have frustum shape.
10. A generalized Voronoi model including the Voronoi spheroidal model, explains how the presence of scutoids in any curved tissue is linked to the surface ratio anisotropy. For any spherical tissue, this anisotropy is null, and the number of scutoids should be 0, being only composed by frustum cells. And as our results indicate: the higher the anisotropy of our models (*Sphere* < *Globe* < *Zeppelin* < *Tube*), the larger the proportion of scutoids, being the tubular geometry the one that allows more scutoids.

ANNEXE

Supplementary tables

	angles ("Transition" vs "No transition")		length "Transition" vs "No transition")	
	h	p	h	p
Salivary Gland	1	4.98E-19	1	3.03E-21
Tubular model - surface ratio 1/0.8	1	2.26E-36	1	7.69E-62
Tubular model - surface ratio 1/0.6	1	1.30E-23	1	2.93E-39
Tubular model - surface ratio 2	1	6.93E-28	1	1.10E-17
Tubular model - surface ratio 5	1	5.36E-15	1	1.74E-06
Embryo surface	0	0.427	1	0.004
Embryo fold	1	3.19E-08	0	0.446
Egg chamber Stage 4	0	0.121	1	3.12E-14
Egg chamber Stage 8	1	0.012	1	2.22E-09
Spheroid Model Stage 4	1	1.06E-112	1	2.82E-263
Spheroid Model Stage 8	1	1.60E-67	1	2.42E-149
Zebrafish	0	0.582	1	0.000

h=1 reject the null hypothesis in which both samples belong to the same distribution

Table 1. Statistic test comparing the edge length and angle distributions differentiating between 'transitions' and 'no transition' edges.

The Kolmogorov Smirnov test was carried out to the measurements of Voronoi models and biological samples.

	R1 mean	R1 std	R2 mean	R2 std	k1 mean	k1 std	k2 mean	k2 std
spheroid s4 - apical	1,497	0,109	0,978	0,024	0,672	0,053	1,023	0,026
spheroid s4 - basal Ch 0.2	1,708	0,107	1,198	0,026	0,588	0,039	0,835	0,018
spheroid s8 - apical	4,080	0,642	0,952	0,053	0,253	0,049	1,054	0,063
spheroid s8 - basal Ch 0.14	4,080	0,614	1,093	0,058	0,252	0,046	0,918	0,052
Globe - apical	2,041	0,223	0,967	0,037	0,497	0,062	1,036	0,041
Globe - basal Ch 0.5	2,470	0,211	1,461	0,043	0,408	0,038	0,685	0,021
Globe - basal Ch 1	2,934	0,205	1,957	0,047	0,343	0,026	0,511	0,013
Globe - basal Ch 2	3,898	0,199	2,953	0,051	0,257	0,014	0,339	0,006
Zeppelin - apical	3,505	0,525	0,954	0,051	0,293	0,053	1,051	0,060
Zeppelin - basal Ch 0.5	3,723	0,472	1,442	0,064	0,274	0,040	0,695	0,033
Zeppelin - basal Ch 1	4,082	0,446	1,933	0,074	0,248	0,031	0,518	0,021
Zeppelin - basal Ch 2	4,940	0,421	2,922	0,086	0,204	0,019	0,343	0,010
Sphere - apical	1	0	1	0	1	0	1	0
Sphere - basal Ch 0.5	1,5	0	1,5	0	0,667	0	0,667	0
Sphere - basal Ch 1	2	0	2	0	0,5	0	0,5	0
Sphere - basal Ch 2	3	0	3	0	0,333	0	0,333	0
tubular model - SR 1	1	0	infinite	0	1	0	0	0
tubular model - SR 1.1111	1,111	0	infinite	0	0,9	0	0	0
tubular model - SR 1.25	1,25	0	infinite	0	0,8	0	0	0
tubular model - SR 1.4286	1,429	0	infinite	0	0,7	0	0	0
tubular model - SR 1.6667	1,667	0	infinite	0	0,6	0	0	0
tubular model - SR 2	2	0	infinite	0	0,5	0	0	0
tubular model - SR 2.5	2,5	0	infinite	0	0,4	0	0	0
tubular model - SR 3.3333	3,333	0	infinite	0	0,3	0	0	0
tubular model - SR 5	5	0	infinite	0	0,2	0	0	0
tubular model - SR 10	10	0	infinite	0	0,1	0	0	0

	Inner surface radii		
	X	Y	Z
Sphere	1	1	1
Globe	1,5	1	1
Zeppelin	2	1	1
Spheroid s4	1,2	1	1
Spheroid s8	2,1	1	1

Table 2. Cauchy curvatures on the Voronoi models.

R1, the maximum radius of Cauchy curvature. R2, the minimum radius of Cauchy curvature. k1, curvature ($1/R1$). k2, curvature ($1/R2$). Ch, cells height.

	mean % scutoids	std % scutoids	mean total cells in ROI	std total cells in ROI
Sphere - Ch 0.5	0,0%	0,0%	97,6	2,5
Sphere - Ch 1	0,0%	0,0%	97,6	2,5
Sphere - Ch 2	0,0%	0,0%	97,6	2,5
Globe - Ch 0.5	21,7%	6,7%	77,0	1,8
Globe - Ch 1	43,5%	7,7%	77,0	1,8
Globe - Ch 2	61,6%	10,1%	77,0	1,8
Zeppelin - Ch 0.5	40,2%	9,3%	54,0	2,7
Zeppelin - Ch 1	68,7%	9,2%	54,0	2,7
Zeppelin - Ch 2	89,2%	5,1%	54,0	2,7
Spheroid s4 - Ch 0.2	6,3%	3,4%	117,7	2,9
Spheroid s8 - Ch 0.14	10,5%	3,5%	236,4	4,9

Table 3. Voronoi spheroidal models sizes and percentage of scutoids.

Extracted data from every Voronoi spheroidal model: Voronoi spheroidal model Stages 4 (s4) and 8 (s8), Sphere, Globe and Zeppelin. Ch (cells height).

BIBLIOGRAPHY

- Adams, M. D., Celniker, S. E., Holt, R. A., Evans, C. A., Gocayne, J. D., Amanatides, P. G., Scherer, S. E., Li, P. W., Hoskins, R. A., Galle, R. F., et al.** (2000). The genome sequence of *Drosophila melanogaster*. *Science* (80-.). **287**, 2185–2195.
- Aegerter-Wilmsen, T., Smith, A. C., Christen, A. J., Aegerter, C. M., Hafen, E. and Basler, K.** (2010). Exploring the effects of mechanical feedback on epithelial topology. *Development* **137**, 499–506.
- Aland, S., Hatzikirou, H., Lowengrub, J. and Voigt, A.** (2015). A Mechanistic Collective Cell Model for Epithelial Colony Growth and Contact Inhibition. *Biophys. J.* **109**, 1347–1357.
- Alberts, B., Johnson, A., Lewis, J., Raff, M., Roberts, K. and Walter, P.** (2015). Molecular biology of the cell, 6th edition by B. Alberts, A. Johnson, J. Lewis, M. Raff, K. Roberts, and P. Walter. In *Biochemistry and Molecular Biology Education*, p. 171.
- Andrew, D. J., Henderson, K. D. and Seshiah, P.** (2000). Salivary gland development in *Drosophila melanogaster*. *Mech. Dev.* **92**, 5–17.
- Arganda-Carreras, I., Kaynig, V., Rueden, C., Eliceiri, K. W., Schindelin, J., Cardona, A. and Seung, H. S.** (2017). Trainable Weka Segmentation: A machine learning tool for microscopy pixel classification. *Bioinformatics* **33**, 2424–2426.
- Artavanis-Tsakonas, S., Rand, M. D. and Lake, R. J.** (1999). Notch signaling: Cell fate control and signal integration in development. *Science* (80-.). **284**, 770–776.
- Axelrod, J. D.** (2006). Cell Shape in Proliferating Epithelia: A Multifaceted Problem. *Cell* **126**, 643–645.
- Bektas, S.** (2017). Curvature of the Ellipsoid with Cartesian Coordinates. *Landsc. Archit. Reg. Plan.* **2**, 61–66.
- Bertet, C., Sulak, L. and Lecuit, T.** (2004). Myosin-dependent junction remodelling controls planar cell intercalation and axis elongation. *Nature* **429**, 667–671.
- Bi, D., Lopez, J. H., Schwarz, J. M. and Manning, M. L.** (2015). A density-independent rigidity transition in biological tissues. *Nat. Phys.* **11**, 1074–1079.
- Bi, D., Yang, X., Marchetti, M. C. and Manning, M. L.** (2016). Motility-driven glass and jamming transitions in biological tissues. *Phys. Rev. X* **6**, 021011.
- Bier, E.** (2005). *Drosophila*, the golden bug, emerges as a tool for human genetics. *Nat. Rev. Genet.* **6**, 9–23.
- Bulgakova, N. A., Klapholz, B. and Brown, N. H.** (2012). Cell adhesion in *Drosophila*: versatility of cadherin and integrin complexes during development. *Curr. Opin. Cell Biol.* **24**, 702–712.
- Canela-Xandri, O., Sagués, F., Casademunt, J. and Buceta, J.** (2011). Dynamics and mechanical stability of the developing dorsoventral organizer of the wing imaginal disc. *PLoS Comput. Biol.* **7**, e1002153.
- Cetera, M. and Horne-Badovinac, S.** (2015). Round and round gets you somewhere: Collective cell migration and planar polarity in elongating *Drosophila* egg chambers. *Curr. Opin. Genet. Dev.* **32**, 10–15.
- Chen, H. H. and Brodland, G. W.** (2000). Cell-level finite element studies of viscous cells in planar aggregates. *J. Biomech. Eng.* **122**, 394–401.

- Chichilnisky, E. J.** (1986). A mathematical model of pattern formation. *J. Theor. Biol.* **123**, 81–101.
- Classen, A. K., Anderson, K. I., Marois, E. and Eaton, S.** (2005). Hexagonal packing of *Drosophila* wing epithelial cells by the planar cell polarity pathway. *Dev. Cell* **9**, 805–817.
- Clevers, H.** (2016). Modeling Development and Disease with Organoids. *Cell* **165**, 1586–1597.
- Collinet, C., Rauzi, M., Lenne, P. F. and Lecuit, T.** (2015). Local and tissue-scale forces drive oriented junction growth during tissue extension. *Nat. Cell Biol.* **17**, 1247.
- Condic, M. L., Fristrom, D. and Fristrom, J. W.** (1991). Apical cell shape changes during *Drosophila* imaginal leg disc elongation: a novel morphogenetic mechanism. *Development* **111**, 23–33.
- Coutelis, J. B. and Ephrussi, A.** (2007). Rab6 mediates membrane organization and determinant localization during *Drosophila* oogenesis. *Development* **134**, 1419–1430.
- Curran, S., Strandkvist, C., Bathmann, J., de Gennes, M., Kabla, A., Salbreux, G. and Baum, B.** (2017). Myosin II Controls Junction Fluctuations to Guide Epithelial Tissue Ordering. *Dev. Cell* **43**, 480–492.
- Dahmann, C.** (2008). *Drosophila*. Humana Press.
- Davidson, L. A. and Davidson, L. A.** (2012). Epithelial machines that shape the embryo. *Trends Cell Biol.* **22**, 82–7.
- Escudero, L. M., da F. Costa, L., Kicheva, A., Briscoe, J., Freeman, M. and Babu, M. M.** (2011). Epithelial organisation revealed by a network of cellular contacts. *Nat. Commun.* **2**, 526.
- Euler, L.** (1767). *Solutio facilis problematum quorundam geometricorum difficillimorum*. Novi Commentarii academiae scientiarum Petropolitanae.
- Farhadifar, R., Roper, J. C., Aigouy, B., Eaton, S. and Julicher, F.** (2007). The influence of cell mechanics, cell-cell interactions, and proliferation on epithelial packing. *Curr Biol* **17**, 2095–2104.
- Fletcher, A. G., Osterfield, M., Baker, R. E. and Shvartsman, S. Y.** (2014). Vertex models of epithelial morphogenesis. *Biophys. J.* **106**, 2291–2304.
- Gates, J.** (2012). *Drosophila* egg chamber elongation insights into how tissues and organs are shaped. *Fly (Austin)*. **6**, 213–227.
- Gibson, W. T. and Gibson, M. C.** (2009). Chapter 4 Cell Topology, Geometry, and Morphogenesis in Proliferating Epithelia. *Curr. Top. Dev. Biol.* **89**, 87–114.
- Gibson, M. C., Patel, A. B., Nagpal, R. and Perrimon, N.** (2006). The emergence of geometric order in proliferating metazoan epithelia. *Nature* **442**, 1038–1041.
- Gilbert, S. F. and Barresi, M. J. F.** (2013). Developmental Biology. *Dev. Biol.*
- Gómez-Gálvez, P., Vicente-Munuera, P., Tagua, A., Forja, C., Castro, A. M., Letrán, M., Valencia-Expósito, A., Grima, C., Bermúdez-Gallardo, M., Serrano-Pérez-Higueras, Ó., et al.** (2018). Scutoids are a geometrical solution to three-dimensional packing of epithelia. *Nat. Commun.* **9**, 2960.
- Goodwin, K. and Nelson, C. M.** (2017). Generating tissue topology through remodeling of cell-cell adhesions. *Exp. Cell Res.* **358**, 45–51.

- Gramates, L. S., Marygold, S. J., Dos Santos, G., Urbano, J. M., Antonazzo, G., Matthews, B. B., Rey, A. J., Tabone, C. J., Crosby, M. A., Emmert, D. B., et al.** (2017). FlyBase at 25: Looking to the future. *Nucleic Acids Res.* **45**, D663–D671.
- Grima, C. I. and Márquez, A.** (2001). *Computational Geometry on Surfaces*. Dordrecht: Springer Netherlands.
- Haeckel, E.** (1904). *Kunstformen der Natur*. Bibliographisches Institut, Leipzig and Vienna.
- Hannezo, E., Prost, J. and Joanny, J. F.** (2014). Theory of epithelial sheet morphology in three dimensions. *Proc. Natl. Acad. Sci. U. S. A.* **111**, 27–32.
- Hardin, J. and Walston, T.** (2004). Models of morphogenesis: The mechanisms and mechanics of cell rearrangement. *Curr. Opin. Genet. Dev.* **14**, 399–406.
- Hayashi, T. and Carthew, R. W.** (2004). Surface mechanics mediate pattern formation in the developing retina. *Nature* **431**, 647–652.
- Heller, D., Hoppe, A., Restrepo, S., Gatti, L., Tournier, A. L., Tapon, N., Basler, K. and Mao, Y.** (2016). EpiTools: An Open-Source Image Analysis Toolkit for Quantifying Epithelial Growth Dynamics. *Dev. Cell* **36**, 103–116.
- Hendow, E. K., Guhmann, P., Wright, B., Sofokleous, P., Parmar, N. and Day, R. M.** (2016). Biomaterials for hollow organ tissue engineering. *Fibrogenesis Tissue Repair* **9**, 3.
- Hočevár, A., El Shawish, S. and Zihlerl, P.** (2010). Morphometry and structure of natural random tilings. *Eur. Phys. J. E* **33**, 369–375.
- Honda, H.** (1978). Description of cellular patterns by Dirichlet domains: the two-dimensional case. *J Theor Biol* **72**, 523–543.
- Honda, H., Nagai, T. and Tanemura, M.** (2008). Two different mechanisms of planar cell intercalation leading to tissue elongation. *Dev. Dyn.* **237**, 1826–1836.
- Huch, M., Knoblich, J. A., Lutolf, M. P. and Martinez-Arias, A.** (2017). The hope and the hype of organoid research. *Development* **144**, 938–941.
- Jang, A. C. C., Starz-Gaiano, M. and Montell, D. J.** (2007). Modeling migration and metastasis in *Drosophila*. *J. Mammary Gland Biol. Neoplasia* **12**, 103–114.
- Jennings, B. H.** (2011). *Drosophila*-a versatile model in biology & medicine. *Mater. Today* **14**, 190–195.
- Jia, D., Xu, Q., Xie, Q., Mio, W. and Deng, W. M.** (2016). Automatic stage identification of *Drosophila* egg chamber based on DAPI images. *Sci. Rep.* **6**, 18850.
- Jiménez, L. F. and Merchant, H.** (2003). *Biología celular y molecular*. Pearson educación.
- Kahle, W., Platzer, W., Fritsch, H., Kühnel, W. and Frotscher, M.** (2013). Color atlas of human anatomy. p. 22.
- Khan, Z., Wang, Y.-C., Wieschaus, E. F. and Kaschube, M.** (2014). Quantitative 4D analyses of epithelial folding during *Drosophila* gastrulation. *Development* **141**, 2895–2900.
- Kim, H. Y., Varner, V. D. and Nelson, C. M.** (2013). Apical constriction initiates new bud formation during monopodial branching of the embryonic chicken lung. *Development* **140**, 3146–3155.
- Kokic, M., Iannini, A., Villa-Fombuena, G., Casares, F. and Iber, D.** (2019). Minimisation of

- surface energy drives apical epithelial organisation and gives rise to Lewis' law. *bioRxiv* 590729.
- Kondo, T. and Hayashi, S.** (2015). Mechanisms of cell height changes that mediate epithelial invagination. *Dev. Growth Differ.* **57**, 313–323.
- Kong, D., Wolf, F. and Großhans, J.** (2017). Forces directing germ-band extension in *Drosophila* embryos. *Mech. Dev.* **144**, 11–22.
- Korn, R. W. and Spalding, R. M.** (1973). The geometry of plant epidermal cells. *New Phytol.* **72**, 1357–1365.
- Latorre, E., Kale, S., Casares, L., Gómez-González, M., Uroz, M., Valon, L., Nair, R. V., Garreta, E., Montserrat, N., del Campo, A., et al.** (2018). Active superelasticity in three-dimensional epithelia of controlled shape. *Nature* **563**, 203.
- Lecuit, T. and Lenne, P. F.** (2007). Cell surface mechanics and the control of cell shape, tissue patterns and morphogenesis. *Nat Rev Mol Cell Biol* **8**, 633–644.
- Lecuit, T. and Wieschaus, E.** (2002). Junctions as organizing centers in epithelial cells? A fly perspective. *Traffic* **3**, 92–97.
- Lecuit, T., Lenne, P.-F. and Munro, E.** (2011). Force Generation, Transmission, and Integration during Cell and Tissue Morphogenesis. *Annu. Rev. Cell Dev. Biol.* **27**, 157–184.
- Lewellyn, L., Cetera, M. and Horne-Badovinac, S.** (2013). Misshapen decreases integrin levels to promote epithelial motility and planar polarity in *Drosophila*. *J. Cell Biol.* **200**, 721–729.
- Lewis, F. T.** (1928). The correlation between cell division and the shapes and sizes of prismatic cells in the epidermis of cucumis. *Anatom. Rec.* **38**, 341–376.
- Lloyd, S.** (1982). Least squares quantization in PCM. *IEEE Trans. Inf. Theory* **28**, 129–137.
- Mao, Y., Tournier, A. L., Hoppe, A., Kester, L., Thompson, B. J. and Tapon, N.** (2013). Differential proliferation rates generate patterns of mechanical tension that orient tissue growth. *EMBO J.* **32**, 2790–2803.
- Messal, H. A., Alt, S., Ferreira, R. M. M., Gribben, C., Wang, V. M.-Y., Cotoi, C. G., Salbreux, G. and Behrens, A.** (2019). Tissue curvature and apicobasal mechanical tension imbalance instruct cancer morphogenesis. *Nature* **566**, 126.
- Monier, B., Gettings, M., Gay, G., Mangeat, T., Schott, S., Guarner, A. and Suzanne, M.** (2015). Apico-basal forces exerted by apoptotic cells drive epithelium folding. *Nature* **518**, 245–248.
- Mughal, A., Cox, S. J., Weaire, D., Burke, S. R. and Hutzler, S.** (2018). Demonstration and interpretation of 'scutoid' cells formed in a quasi-2D soap froth. *Philos. Mag. Lett.* **98**, 358–364.
- Nelson, C. M.** (2016). On buckling morphogenesis. *J. Biomech. Eng.* **138**, 021005.
- O'Toole, M. T.** (2009). Mosby's dictionary of medicine, nursing & health professions. *Choice Rev. Online* **47**, 47-0623-47-0623.
- Okuda, S., Miura, T., Inoue, Y., Adachi, T. and Eiraku, M.** (2018). Combining Turing and 3D vertex models reproduces autonomous multicellular morphogenesis with undulation, tubulation, and branching. *Sci. Rep.* **8**.
- Osterfield, M., Du, X. X., Schüpbach, T., Wieschaus, E. and Shvartsman, S. Y.** (2013). Three-

- Dimensional Epithelial Morphogenesis in the Developing *Drosophila* Egg. *Dev. Cell* **24**, 400–410.
- Pearl, E. J., Li, J. and Green, J. B. A.** (2017). Cellular systems for epithelial invagination. *Philos. Trans. R. Soc. B Biol. Sci.* **372**, 20150526.
- Reinhardt, K.** (1918). Über die Zerlegung der Ebene in Polygone.
- Rodriguez-Arnaiz, R., Ramos Morales, P. and Zimmering, S.** (1992). Evaluation in *Drosophila melanogaster* of the mutagenic potential of furfural in the mei-9a test for chromosome loss in germ-line cells and the wing spot test for mutational activity in somatic cells. *Mutat. Res. Toxicol.* **280**, 75–80.
- Ross, M. H. and Pawlina, W.** (2012). *Histología : texto y atlas color con biología celular y molecular*. 6th ed. Editorial Médica Panamericana.
- Rupprecht, J.-F., Ong, K. H., Yin, J., Huang, A., Dinh, H.-H.-Q., Singh, A. P., Zhang, S., Yu, W. and Saunders, T. E.** (2017). Geometric constraints alter cell arrangements within curved epithelial tissues. *Mol. Biol. Cell* **28**, 3582–3594.
- Sanchez-Corrales, Y. E., Blanchard, G. B. and Röper, K.** (2018). Radially patterned cell behaviours during tube budding from an epithelium. *Elife* **7**,.
- Sanchez-Gutierrez, D., Tozluoglu, M., Barry, J. D., Pascual, A., Mao, Y. and Escudero, L. M.** (2016). Fundamental physical cellular constraints drive self-organization of tissues. **35**, 77–88.
- Schindelin, J., Arganda-Carreras, I., Frise, E., Kaynig, V., Longair, M., Pietzsch, T., Preibisch, S., Rueden, C., Saalfeld, S., Schmid, B., et al.** (2012). Fiji: an open-source platform for biological-image analysis. *Nat. Methods* **9**, 676–682.
- Schneider, P. J. and Eberly, D. H.** (2003). *Geometric tools for computer graphics, chapter 10*. Elsevier Science (USA).
- Shraiman, B. I.** (2005). Mechanical feedback as a possible regulator of tissue growth. *Proc. Natl. Acad. Sci. U. S. A.* **102**, 3318–3323.
- Spencer, M. A., Jabeen, Z. and Lubensky, D. K.** (2017). Vertex stability and topological transitions in vertex models of foams and epithelia. *Eur. Phys. J. E* **40**, 2.
- Spradling, A. C.** (1993). Developmental genetics of oogenesis. In *The Development of Drosophila melanogaster*, p. Cold Spring Harbor Laboratory Press.
- Stevens, P. S.** (1974). *Patterns in Nature*. Boston-Toronto: Little Brown and Co. in association with The Atlantic Monthly Press.
- Štorgel, N., Krajnc, M., Mrak, P., Štrus, J. and Zihler, P.** (2016). Quantitative Morphology of Epithelial Folds. *Biophys. J.* **110**, 269–277.
- Sun, Z., Amourda, C., Shagirov, M., Hara, Y., Saunders, T. E. and Toyama, Y.** (2017). Basolateral protrusion and apical contraction cooperatively drive *Drosophila* germ-band extension. *Nat. Cell Biol.* **19**, 375–383.
- Tortora, G. J. and Derrickson, B.** (2018). *Principios de anatomía y fisiología*. Médica Panamericana.
- Vaccari, T., Lu, H., Kanwar, R., Fortini, M. E. and Bilder, D.** (2008). Endosomal entry regulates Notch receptor activation in *Drosophila melanogaster*. *J. Cell Biol.* **180**, 755–762.

- Vicente-Munuera, P., Gómez-Gálvez, P., Tetley, R. J., Forja, C., Tagua, A., Letrán, M., Tozluoglu, M., Mao, Y. and Escudero, L. M.** (2019a). EpiGraph: an open-source platform to quantify epithelial organization. *bioRxiv* 217521.
- Vicente-Munuera, P., Gómez-Gálvez, P., Tetley, R. J., Forja, C., Tagua, A., Letrán, M., Tozluoglu, M., Mao, Y. and Escudero, L. M.** (2019b). EpiGraph: an open-source platform to quantify epithelial organization. *Bioinformatics*.
- Villanueva, A. R., López, C. and Ruiz, A.** (2003). *Diccionario Mosby de Medicina , Enfermería y Ciencias de la Salud , 6ª ed . Códex del Laboratorio Clínico . Indicaciones e interpretación de los exámenes de laboratorio.*
- Voronoi, G.** (1908). Nouvelles applications des paramètres continus à la théorie des formes quadratiques. Deuxième mémoire. Recherches sur les paralléloèdres primitifs. *J. für die reine und Angew. Math.* **134**, 198–287.
- Weigmann, K., Klapper, R., Strasser, T., Rickert, C., Technau, G., Jäckle, H., Janning, W. and Klämbt, C.** (2003). FlyMove – a new way to look at development of *Drosophila*. *Trends Genet.* **19**, 310–311.
- Welsch, U., Sobotta, J. and Delles, T.** (2014). *Histología*. Médica Panamericana.
- Wetzel, G.** (1926). Zur entwicklungsmechanischen Analyse des einfachen prismatischen Epithels. *Wilhelm Roux Arch. für Entwicklungsmechanik der Org.*
- Xu, B., Washington, A. M., Domeniconi, R. F., Ferreira Souza, A. C., Lu, X., Sutherland, A. and Hinton, B. T.** (2016). Protein tyrosine kinase 7 is essential for tubular morphogenesis of the Wolffian duct. *Dev. Biol.* **412**, 219–233.
- Yin, X., Mead, B. E., Safaee, H., Langer, R., Karp, J. M. and Levy, O.** (2016). Engineering Stem Cell Organoids. *Cell Stem Cell* **18**, 25–38.
- Zallen, J. A. and Zallen, R.** (2004). Cell-pattern disordering during convergent extension in *Drosophila*. *J. Phys. Condens. Matter* **16**, 5073–5080.
- Zhu, H. X., Thorpe, S. M. and Windle, A. H.** (2001). The geometrical properties of irregular two-dimensional Voronoi tessellations. *Philos. Mag. A Phys. Condens. Matter, Struct. Defects Mech. Prop.* **81**, 2765–2783.

